UNIVERSITÀ DEGLI STUDI DI PADOVA

SCUOLA DI INGEGNERIA

*Corso di Laurea in Ingegneria dei Materiali*

# FRACTURE ASSESSMENT OF ENGINEERING MATERIALS UNDER MIXED MODE LOADING BY MEANS OF LOCAL APPROACHES

*Laureando*
**Giacomo Maculan**

*Relatore*
**Prof. Paolo Ferro**

*Co-Relatori*
**Prof. Filippo Berto**
**S.M. Javad Razavi**

ANNO ACCADEMICO 2017/2018

# Contents

# Abstract

Fracture of materials weakened by cracks is a topic that has drawn the attention of many researchers since the early years of the last century, and represents nowadays a fundamental subject of study, considered both by academic and industrial world.

In particular, brittle failure of components is an attractive phenomenon that concerns a large number of applications in different discipline of engineering: the problem of fracture of materials has to be taken into account in every technological device, whether or not it performs a purely mechanical function. For instance, the employment of new advanced materials in thermal, optical or electronic applications, often cannot be realized regardless of an appropriate mechanical design that ensure the structural integrity of the material.

Specifically, the topic of fracture is significantly important in the presence of intrinsic defects of the material, or different type of geometrical discontinuities. Such entities give rise to localized stress concentration, which may result in crack growing phenomenon and hence to catastrophic failure or to a reduction of the assessed structural life. These circumstances, where stress concentration effects take place in the component, require the employment of advanced design approaches which are the results of several decades of intensive research on fracture phenomena.

It is interesting to note that while cracks are surely unpleasant entities in almost every case of engineering material, notches of different shape and size are often deliberately introduced in structural components to fulfill design or manufacturing requirements. This means that the use of fracture mechanics principles is not necessarily restricted to the case of damaged components, but rather pertains to a large number of practical cases including, for example, welding, adhesive or bolted joints.

The purpose of this work is to apply one of the current methods for the fracture assessment of materials, namely the ASED (Averaged Strain Energy Density) criterion, by numerical modelling of several experimental scenarios. The software employed is ANSYS 16.2, and the approach adopted consists in the geometrical modelling and finite elements analysis of several experimental tests by writing dedicated APDL (Ansys Parametric Design Language) codes. The aim of every numerical model is to provide a failure prediction of different materials in terms of critical applied load.

Particular attention is given to the investigation of different mode of loading, which results in some extensions of the conventional failure criterion that are discussed and presented in this work.

This thesis is divided into five chapters. The first chapter serves as an introduction to fracture mechanics and its relevant research achievements, from the early study of cracks, to the more recent case of notches, followed by the presentation of the most common failure assessment criteria currently in use.

The second chapter is dedicated to the explanation of the most remarkable fracture mechanics theories which create the basement for the failure criterion employed in this work. The most important concepts, definitions and analytical expressions useful for the understanding of the method are presented.

In the third chapter the ASED method is explained in detail. Particular attention is given to discuss the fundamental hypothesis and the analytical derivation of the most important equations.

The fourth chapter illustrates the finite element procedure implemented in this work. We introduce here the experimental scenarios and the creation of the relative numerical models, describing all the choices and assumptions adopted for the implementation of numerical code. Most importantly, alternative procedures for the failure evaluation of materials under study are here proposed.

The last chapters collects all the numerical results obtained by a substantial number of finite elements analysis. The relevant fracture parameters including the failure prediction of materials are presented and discussed by comparison with experimental data available in literature.

# Chapter 1

# Introduction

In this chapter, the topic of fracture mechanics is introduced. At the beginning, we discuss the phenomenon of failure of materials and how it affected society, from the time of first civilizations to the period of industrial revolution. In parallel, a brief overview regarding how this branch of engineering study developed over the years is supplied by mentioning some of the major research achievements that created the basis for this new theory. Finally, the most important methods currently in use for the assessment of failure of materials are listed.

## 1.1 Importance of fracture mechanics

Fracture is a phenomenon that has affected society for many centuries, as long as there have been man-made structures. The problem of brittle fracture represents a topic of big concern with regards to the structural integrity assessment of mechanical components because of its catastrophic nature: annual cost in U.S. due to fracture failures was estimated at $119 billion in 1978 [1], corresponding to about 4% of the gross national product.

However, the knowledge of materials failure became relevant only after the World War II, when the strong development of sophisticated structures demanded new designing criteria which took into account fracture mechanics principles.

Before the time of Isaac Newton, when the knowledge of mechanics was relatively limited, architecture and engineering designs were probably achieved mainly by trial and error. Nevertheless, since the time of Egyptians and Romans until the Industrial Revolution the primary materials practical for construction were timber, brick and mortar; only the latter two were employed for large building, such as cathedrals or bridges, given that trees of sufficient size for support beams were uncommon.

Despite the brittle behavior of brick and mortar, the structural integrity was achieved designing structures to be loaded in compression rather than in tension, which explains the durability of ancient structures such as Egyptian pyramids and Roman arches.

It is only during the 19th century, with the advent of industrial revolution, that materials such as iron and steel started to be produced massively, and the design restrictions typical of structures operative under compression loading were removed [2].

If in one hand the change from brick and mortar structures loaded in compression to ductile steel structures loaded in tension turned into a more flexible design, in the other it brought some problems: occasionally, catastrophic failures occurred at stresses well below the expected tensile strength.

A report dated 1954 [3] describes several cases of steel structures, including bridges, pressure vessel and pipelines, that undergo brittle fracture phenomena, meaning that new and more complex models for the description of the mechanical behavior of materials were needed.

While in the previous years the strength assessment of components assumed as a fundamental point the structural integrity of the materials, after the World War II new designing approaches were developed, where the presence of cracks and defects were included as initial hypothesis.

More recently, on the basis of fracture mechanics theories of cracked components, researchers focused in another novel field of solid mechanics, namely, notch mechanics. Here the formulations first applied to the case of cracked materials were extended to study the more complex case of notched components.

Nowadays, the study of structures weakened by stress concentrator factors like cracks and notches assumed a primary role in engineering design methods, especially for those components with high safety standards typical of marine, aerospace or civil structures. Nevertheless, the establishment of notch mechanics as an advanced engineering tool in mechanical design has been strongly encouraged by the parallel development of software dedicated to the finite elements analysis. Precisely, at the state of the art, the majority of the failure evaluations by means of fracture mechanics is carried out through a large use of numerical models.

However, while new criteria of failure by means of fracture mechanics principles were established in designing practice during the last decades, the estimation of brittle fracture in components containing different type of notches and cracks required effective theories that are still not completely understood.

## 1.2 Fracture research

One of the primordial attempts to assess the strength of materials is due to Leonardo da Vinci [4], when in his experimental work he studied the influence of flaws on the mechanic behavior of iron wires.

From those qualitative results, however, it passed several centuries after a quantitative connection between fracture stress and flaw size was proposed by Griffith [5] in 1920.

Griffith, on the basis of the stress field around an elliptical hole derived by Inglis [6] in 1913, developed a criterion of crack propagation based on an energy balance: the crack propagates as soon as the strain energy, which results from an increment of the crack size, overcomes the required surface energy.

The model successfully assessed the fracture phenomena of brittle material, such as glass, while did not match the behavior of ductile materials such as steel.

It was only in 1948 that Irwin [8] extended the Griffith approach to metals by means of consideration of the energy dissipated by local plastic flow. In the same year, Orowan independently proposed a similar modification to the Griffith theory [9].

A milestone in fracture mechanics was achieved in 1956 by Irwin [10]. He took into account Westergaard equations (derived in 1938) to describe the stresses and displacements around a sharp crack by means of a single constant related to the energy release rate (as detailed in the next chapter).

In the same period Williams determined the stress field in the vicinity of a sharp notch tip [11, 12], hence extending the results obtained for cracks to the case of notches.

Since the early results by Williams, researchers deeply focused on notch fracture mechanics, an important extension of the classical fracture mechanics from cracks to notch problems. In fact, notched components are susceptible to catastrophic failure because of the stress concentration at the notch tip, and are very diffused in mechanical constructions, representing a topic of fundamental concern in the practice of engineering design.

The next section presents the most important approaches for the fracture assessment of notches developed in the last decades.

## 1.3 Approaches for brittle fracture assessment

Some of the current approaches for brittle fracture assessment of notches are presented in this section. In particular, we discuss here the following methods:

- J-integral method
- Theory of critical distances
- Finite Fracture mechanics
- Averaged strain energy density criterion

### 1.3.1 J-integral

The J-integral represents a method to calculate the strain energy release per unit fracture surface, in a material. This criterion was first introduced by Rice [13] in 1968, who showed that an energetic contour path integral was independent of the path around the crack or the notch. Hence, the main advantage of this approach is to apply a line integral between two points located in the opposite face borders of the crack avoiding the problem of stress singularity at the notch tip [14].

### 1.3.2 Theory of critical distances

According to the theory of critical distances (TCD) the most relevant parameter for the fracture assessment is the so-called intrinsic crack $a_0$, introduced by Smith and Topper in 1979 [15]. The method affirms that failure of mechanical components takes place when the averaged stress over a line (*Line method*) or the stress at a certain distance from the crack tip (*Point method*) is greater than the plain fatigue limit of the material.

The distance at which the stress has to be calculated in order to apply the point method is equal to $a_0/2$ while for the line method stress has to be integrated over a line with length equal to $2a_0$.

### 1.3.3 Finite Fracture mechanics

Finite fracture mechanics (FFM) is a coupled stress and energy failure criterion [16]. According to FFM, crack propagates in the material by finite steps, under the simultaneous fulfilment of two conditions. The first one is a stress requirement, and supposes that the averaged of the stress over the crack step-advancement has to be greater than the material tensile strength. The second conditions implies the accomplishment of an energy balance: the integral of the crack driving force should compensate the required energy for the creation of new fracture surfaces. By applying these conditions at failure conditions, a number of fracture parameters such as the crack extension angle and the generalized fracture toughness can be derived.

### 1.3.4 Averaged strain energy density criterion

The averaged strain energy density (ASED) criterion was formulated and used first for sharp V-notches by Lazzarin and Zambardi [17], and later extended to U-notches and blunt V-notches by Lazzarin and Berto [18]. The ASED criterion states that brittle failure takes place when the average of the SED over a defined control volume, which embraces the notch edge, is equal to a critical SED, $Wc$, varying for different materials.

The idea of a control volume was first developed by Neuber [19]: he claimed that the fatigue behavior of metallic components is rather determined by an averaged stress into a define structural volume than a point wise peak stress. The size of the control volume was thought to be a property of the material.

ASED is the method employed in this work, and will be therefore explained in detailed in the next chapters.

# Chapter 2

# Fracture Mechanics

Fracture mechanics is the field of mechanic that studies the structural integrity of components with the presence of defects. It is a relatively new subject, developed in the last century as an evolution of classics machine design theories.

As a matter of fact, flaws and cracks may arise in materials because of multiple reasons:

- During the employment of the component, because of a bad usage by the user or an erroneous design.
- During the manufacture process. For instance, there could be the presence of porous due to imperfect casting or sintering of metals and ceramics, or improper cohesion between matrix and reinforcement in composites.
- Cracks might be hypothesized during design, especially for components subjected by high safety standard, for example in the field of aeronautical and civil engineering.

In the present chapter, only the case of linear elastic fracture mechanics (LEFM) with isotropic materials is considered. The derivation of stress field in the presence of cracks is explained and the relevant parameters defining failure criteria are presented. Successively, basic concepts are expanded by defining different modes of fracture and introducing the case of sharp V-notches. Finally, a mathematical analytical procedure to describe stresses in the case of defected materials is first presented in the case of plane problems and next extended to the case of out of plane loading conditions.

## 2.1 Stress analysis

To understand the problem of the presence of cracks regarding the stress field assessment it is worthwhile to start from the classical problem of a plate with circular hole loaded under tension in the plane, represented in figure 2.1a.

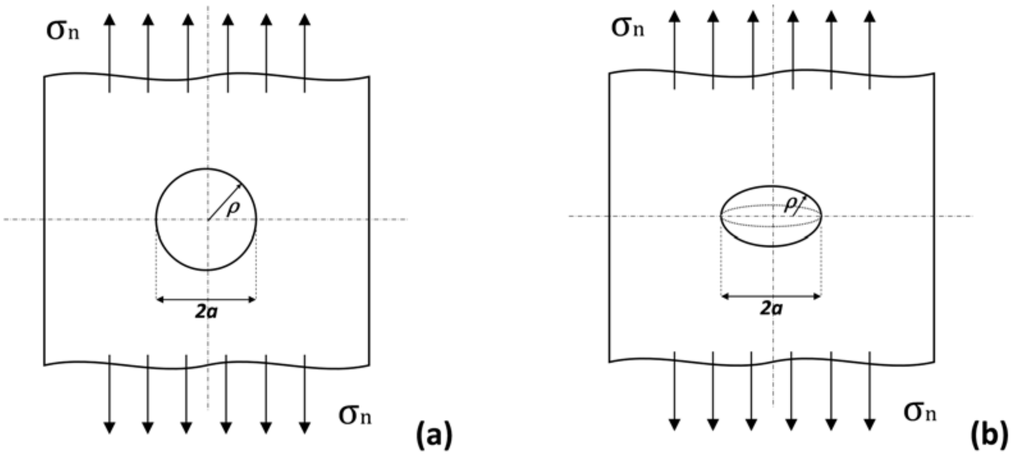

Figure 2.1: Infinite plate with remote tensile load $\sigma_n$ weakened by a circular (a) and an elliptical (b) hole.

The solution of this problems in terms of stresses was first solved by Kirsch in 1898 [7], and it involved the introduction of a stress concentration factor ($K_{tg}$) that accounts for the stress amplification in the vicinity of the hole.

$$\sigma_{pel} = k_{tg} \cdot \sigma_g \tag{2.1}$$

where $\sigma_{pel}$ is the elastic stress peak due to the hole and $\sigma_g$ is the nominal stress calculated in the gross section of the plate. Kirsch found that, in the case of a circular hole like the one represented in figure 2.1a, $k_{tg}$ is equal to 3.

Similarly to this case, is the one with plate weakened by an elliptical hole shown in figure 2.1b. Inglis, in 1913, proposed the following analytical expression for $k_{tg}$ [6]:

$$k_{tg} = 1 + 2\sqrt{\frac{a}{\rho}} \tag{2.2}$$

Where $a$ and $\rho$ are respectively the major semi axe and the radius of the ellipse. Is evident that Kirsch solution is a particular case of the last expression where $a = \rho$.

We can now notice that by shrinking the minor axe of the elliptic hole in figure 2.1b, at the limit conditions, one would have a crack of length $2a$ and $\rho = 0$.

Therefore, according to classic mechanics, the stress concentration factor would be infinite, which fact turns into a singularity of the stress field at the crack tip.

It is evident that the failure criteria of classic mechanics, where the singular stress peak value would have been compared with a limit value, failed when applied to crack components, since experimental evidences show that materials with flaws with approximately zero radius present a certain resistance to loading.

The fundamental proposal of LEFM is to assume that the stress field varies as a homothetic function of the applied stress and has to be compared with a "limit" stress field thought as function of material.

Taking into account the cracked plate and the polar coordinate system in figure 2.2 we present now the expression for the stress field derived by Irwin [10].

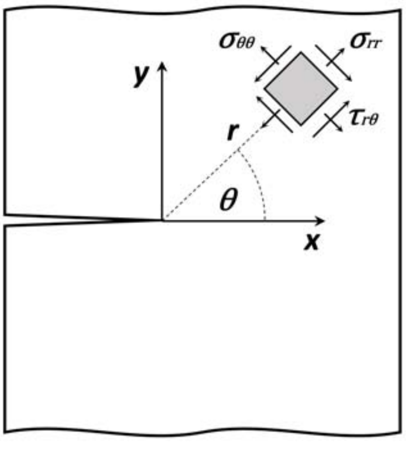

Figure 2.2: Polar coordinate system $(r, \theta)$ centered at the crack tip.

He took advantage of some mathematical derivations for stress field in the vicinity of a crack tip presented by Westergaard 1939 [20] and proposed the following equations:

$$\sigma_{\theta\theta} = \frac{K_I}{4\sqrt{2\pi r}}\left\{\cos\frac{3}{2}\theta + 3\cos\frac{\theta}{2}\right\} \tag{2.3a}$$

$$\sigma_{rr} = \frac{K_I}{4\sqrt{2\pi r}}\left\{-\cos\frac{3}{2}\theta + 5\cos\frac{\theta}{2}\right\} \tag{2.3b}$$

$$\tau_{r\theta} = \frac{K_I}{4\sqrt{2\pi r}}\left\{\sin\frac{3}{2}\theta + \sin\frac{\theta}{2}\right\} \tag{2.3c}$$

where parameter $K_I$ is named mode I *Stress Intensity Factor*, and is defined as follow

$$K_I = \sqrt{2\pi}\lim_{r\to 0^+} r^{\frac{1}{2}}\sigma_{\theta\theta}(r, \theta = 0) \tag{2.4}$$

Irwin's contribution was to give a physical significance to Westergaard's expressions by means of the field parameter $K_I$, showing that the intensity of this singularity is dependent on the magnitude of the relevant structural stresses.

Expressions (2.3) are valid only for mode I loading (the different mode of fracture will be clarified in the next section), plane stress or plane strain conditions, and for moderate remote loading (generally for $\sigma_g < 0.5\sigma_Y$, where $\sigma_Y$ represent the material yield strength).

$K_I$ is a fundamental parameter in LEFM, and accounts for the aforementioned homothetic behavior of the stress field with respect to the external applied load.

## 2.2 Fracture mode

As mentioned before, Irwin expressions (2.3) are valid under mode I loading conditions. To clarify this, we must say now that there are three ways of applying a force to enable a crack to propagate:

- Mode I fracture - Opening mode: a tensile stress normal to the plane of the crack. Figure 2.3a.
- Mode II fracture - Sliding mode: a shear stress acting parallel to the plane of the crack and perpendicular to the crack front). Figure 2.3b.
- Mode III fracture - Tearing mode: a shear stress acting parallel to the plane of the crack and parallel to the crack front. Figure 2.3c.

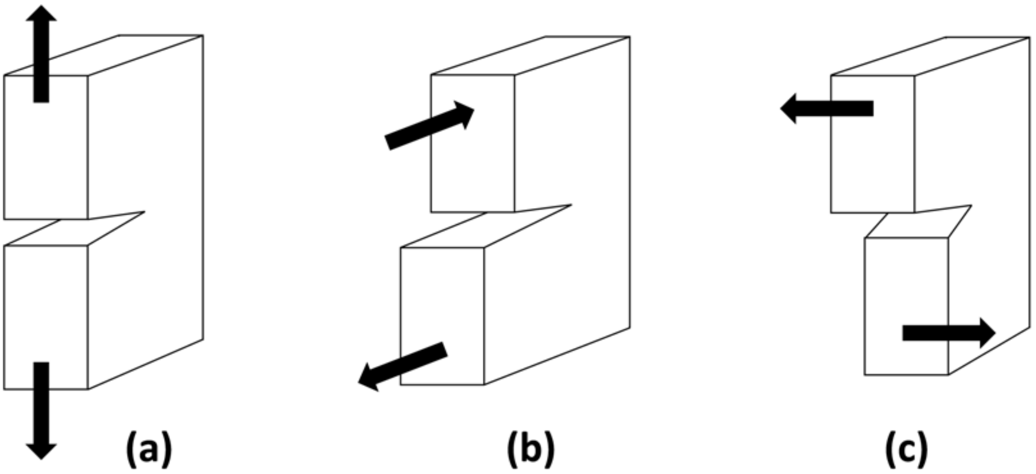

Figure 2.3: Mode of fracture: mode I (a), mode II (b) and mode III (c).

It is worth mention that mode I and mode II constitute the plane problem, while mode III represent an out-of-plane loading condition, as it is clear from figure 2.3.

Moreover, opening mode fracture, related to tensile stress, is symmetric with respect of the crack plane whereas sliding mode, related to shear stresses, is antisymmetric.

As the purpose of this work is the structural assessment under mixed mode loading, in the following sections particular attention will be given to extend the formulations previously mentioned for pure mode I to mode II, mode III and mixed mode fracture.

## 2.3 Extension from crack to V-notch

The extension from cracks to V-notches is due to Williams [11]. He considered a V-notch represented in figure 2.4, where the opening angle $2\alpha$ was different from zero, and analyzed the stress field in the vicinity of the notch tip by means of a particular form of the Airy function, and solved the relative eigenvalues problem for mode I and mode II.

It emerged that, as already seen with cracks, the stress field could be expressed by means of a single parameter which definitions is due to Gross and Mendelson(1972) [21]:

$$K_1 = \sqrt{2\pi} \lim_{r \to 0^+} r^{1-\lambda_1} \sigma_{\theta\theta}(r, \theta = 0) \tag{2.5}$$

$$K_2 = \sqrt{2\pi} \lim_{r \to 0^+} r^{1-\lambda_2} \tau_{r\theta}(r, \theta = 0) \tag{2.6}$$

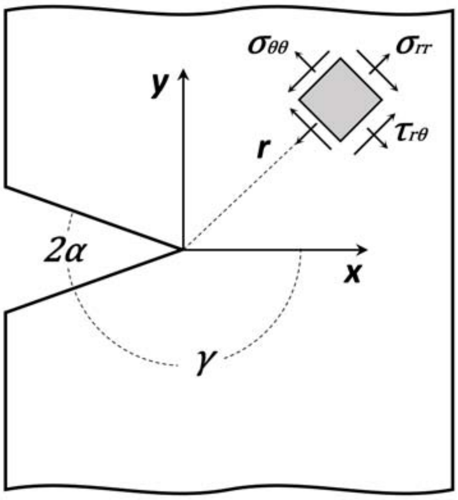

Figure 2.4: Scheme of a sharp V-notch showing the coordinate system centered at the notch tip, the opening angle $2\alpha$ and the angle between the notch bisector and the notch face $\gamma$.

where $\lambda_1$ and $\lambda_2$ are the first eigenvalues for mode I and II problems respectively. The expressions $(1-\lambda)$ is called *singularity degree* and accounts for the stress degree singularity at the notch tip, which mathematical derivation will be explained in the next section. The *singularity degree* was found to vary with the opening angle $2\alpha$ as shown in figure 2.5.

Parameters $K_1$ and $K_2$ were named Notch stress intensity factors (NSIFs) for mode I and II respectively.

It is interesting to note that crack can be seen as a particular case of V-notch with opening angle $2\alpha = 0$, and the value of the singularity degree for pure mode I, equal to 0.5 according to equation (2.4), is found to be consistent with the definition given in (2.5).

With the same meaning of terms, we define here the stress intensity factor ($K_3$) related to mode III loading [22], which will be useful later in this work.

$$K_3 = \sqrt{2\pi} \lim_{r \to 0^+} r^{1-\lambda_3} \tau_{\theta z}(r, \theta = 0) \tag{2.7}$$

## 2.4 Mode I & II: Muskhelishvili formulation

We describe in this section one of the most important method for the evaluation of singular stress field. A Russian mathematician named Muskhelishvili proposed it in literature for the first time in 1953 [23], and gained celebrity within a few months since its publication. However, Muskhelishvili

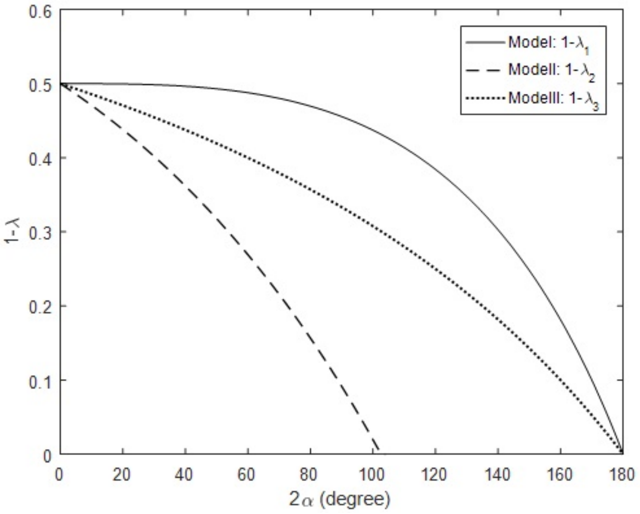

Figure 2.5: Singularity degree $1-\lambda$ for different mode of fracture in function of the notch opening angle $2\alpha$.

affirmed that his theory resumed some concepts taught to him by his professor Kolosov, and therefore the method is better known with the name of Muskhelishvili-Kolosov.

The formulation is based on the employment of complex function potentials to define a particular form of an Airy function, and represents nowadays the most general analytical solution for the analysis of in plane notches and cracks. All other methods in literature, including Westergaard's solution described in the previous section, could be seen as particular cases of the more general Muskhelishvili's solution.

The two fundamental equations of the formulation, expressed in Cartesian coordinates, are shown below

$$\sigma_{xx}+\sigma_{yy}=\frac{\partial^2\Phi}{\partial y^2}+\frac{\partial^2\Phi}{\partial x^2}=2\mathit{\Psi}'(z)+2\overline{\mathit{\Psi}'}(z)=4\,\mathrm{Re}(\mathit{\Psi}'(z)) \tag{2.8a}$$

$$\sigma_{yy}-\sigma_{xx}+2i\tau_{xy}=\frac{\partial^2\Phi}{\partial x^2}-\frac{\partial^2\Phi}{\partial y^2}-2i\frac{\partial^2\Phi}{\partial x\partial y}=2(\overline{z}\mathit{\Psi}''(z)+\varphi''(z)) \tag{2.8b}$$

where $z$ is a complex number, $\Phi$ is the Airy function, while $\mathit{\Psi}$ and $\varphi$ are suitable holomorphic complex functions, to be defined. We write now the previous equations in more convenient polar coordinates:

$$\sigma_{rr} + \sigma_{\theta\theta} = 4\,\mathrm{Re}(\mathit{\Psi}'(z)) \tag{2.9a}$$

$$\sigma_{\theta\theta} - \sigma_{rr} + 2i\tau_{r\theta} = 2e^{2i\theta}(\overline{z}\mathit{\Psi}''(z) + \varphi''(z)) \tag{2.9b}$$

The solution of any in-plane problems is based on these general formulas and derives from the definition of the complex potentials $\mathit{\Psi}$ and $\varphi$ and the application of suitable boundary conditions.

We present here the complex potentials proposed by Lazzarin and Tovo [24] for the analysis of sharp and blunt plane notches.

$$\mathit{\Psi}(z) = az^{\lambda} \tag{2.10}$$

$$\mathit{\Psi}(z) = bz^{\lambda} + cz^{\mu} \tag{2.11}$$

where

$$a, b, c, z \in \mathbb{C} \qquad \lambda, \mu \in \mathbb{R} \qquad \mu < \lambda$$

$$a = a_1 + ia_2 \qquad b = b_1 + ib_2 \qquad c = c_1 + ic_2$$

In order to give a physical meaning to the aforementioned complex potentials, we anticipate here that having complex coefficient $a$, $b$ and $c$ allow to deal separately with mode I and mode II contributions. In particular, subscript 1 ($a_1$, $b_1$, $c_1$) refers to mode I while subscript 2 ($a_2$, $b_2$, $c_2$) stands for mode II.

Moreover, real coefficient $\lambda$ is related to the field stress gradient, as already anticipated speaking about stress field singularity degree in previous sections.

By putting functions (2.10) and (2.11) (and their derivatives) in the fundamental equations (2.9), after several algebraic derivations, one obtains the following expressions for the components of the stress field:

$$\begin{aligned}\sigma_{\theta\theta} =&\lambda r^{\lambda-1}[a_1(1+\lambda)\cos(1-\lambda)\theta + a_2(1+\lambda)\sin(1-\lambda)\theta+\\ &+ b_1\cos(1+\lambda)\theta - b_2\sin(1+\lambda)\theta]+\\ &+ \mu r^{\mu-1}[c_1\cos(1+\mu)\theta - c_2\sin(1+\mu)\theta]\end{aligned} \tag{2.12a}$$

$$\begin{aligned}\sigma_{rr} =&\lambda r^{\lambda-1}[a_1(3-\lambda)\cos(1-\lambda)\theta + a_2(3-\lambda)\sin(1-\lambda)\theta+\\ &- b_1\cos(1+\lambda)\theta + b_2\sin(1+\lambda)\theta]+\\ &+ \mu r^{\mu-1}[-c_1\cos(1+\mu)\theta + c_2\sin(1+\mu)\theta]\end{aligned} \tag{2.12b}$$

$$\begin{aligned}\tau_{r\theta} =&\lambda r^{\lambda-1}[a_1(1-\lambda)\sin(1-\lambda)\theta - a_2(1-\lambda)\cos(1-\lambda)\theta+\\ &+ b_1\sin(1+\lambda)\theta + b_2\cos(1+\lambda)\theta]+\\ &+ \mu r^{\mu-1}[c_1\sin(1+\mu)\theta + c_2\cos(1+\mu)\theta]\end{aligned} \tag{2.12c}$$

We will treat in this work only the case of sharp cracks (i.e. notches with zero notch-radius), that in literature is known as William problem. For this case, a simpler form of the second potential may be used instead of equation (2.11). The proposal of England (1971) [25] was the following

$$\varphi(z) = bz^{\lambda} \tag{2.13}$$

with the same meaning of symbols previously clarified.

By using (2.13) in (2.9) the formulation for the stress components substantially simplify into

$$\begin{aligned}\sigma_{\theta\theta} =&\lambda r^{\lambda-1}[a_1(1+\lambda)\cos(1-\lambda)\theta + a_2(1+\lambda)\sin(1-\lambda)\theta+\\ &+ b_1\cos(1+\lambda)\theta - b_2\sin(1+\lambda)\theta]\end{aligned} \tag{2.14a}$$

$$\begin{aligned}\sigma_{rr} =&\lambda r^{\lambda-1}[a_1(3-\lambda)\cos(1-\lambda)\theta + a_2(3-\lambda)\sin(1-\lambda)\theta+\\ &- b_1\cos(1+\lambda)\theta + b_2\sin(1+\lambda)\theta]\end{aligned} \tag{2.14b}$$

$$\begin{aligned}\tau_{r\theta} =&\lambda r^{\lambda-1}[a_1(1-\lambda)\sin(1-\lambda)\theta - a_2(1-\lambda)\cos(1-\lambda)\theta+\\ &+ b_1\sin(1+\lambda)\theta + b_2\cos(1+\lambda)\theta]\end{aligned} \tag{2.14c}$$

Finally, by taking advantage of the superposition principle, is possible to rewrite equations (2.14) uncoupling mode I and mode II contributions as follows:

$$\begin{pmatrix}\sigma_{\theta\theta}\\ \sigma_{rr}\\ \tau_{r\theta}\end{pmatrix}_I = \lambda r^{\lambda-1} a_1 \left[\begin{pmatrix}(1+\lambda)\cos(1-\lambda)\theta\\ (3-\lambda)\cos(1-\lambda)\theta\\ (1-\lambda)\sin(1-\lambda)\theta\end{pmatrix} + b_1 \begin{pmatrix}\cos(1+\lambda)\theta\\ -\cos(1+\lambda)\theta\\ \sin(1+\lambda)\theta\end{pmatrix}\right] \tag{2.15}$$

$$\begin{pmatrix}\sigma_{\theta\theta}\\ \sigma_{rr}\\ \tau_{r\theta}\end{pmatrix}_{II} = \lambda r^{\lambda-1} a_2 \left[\begin{pmatrix}(1+\lambda)\sin(1-\lambda)\theta\\ (3-\lambda)\sin(1-\lambda)\theta\\ -(1-\lambda)\cos(1-\lambda)\theta\end{pmatrix} + b_2 \begin{pmatrix}-\sin(1+\lambda)\theta\\ \sin(1+\lambda)\theta\\ \cos(1+\lambda)\theta\end{pmatrix}\right] \tag{2.16}$$

where subscript $I$ refers to mode I stress components, while subscript $II$ to mode II ones.

Now, by applying suitable boundary conditions to equations (2.15) and (2.16) (i.e that stress components $\sigma_{\theta\theta}$ and $\tau_{r\theta}$ at the unloaded surface of the notch are equal to zero) one obtains the two following homogeneous systems for mode I and II respectively

$$\begin{bmatrix}(1+\lambda)\cos(1-\lambda)\gamma & \cos(1+\lambda)\gamma\\ (1-\lambda)\sin(1-\lambda)\gamma & \sin(1+\lambda)\gamma\end{bmatrix}\begin{pmatrix}a_1\\ b_1\end{pmatrix} = \begin{bmatrix}0\\ 0\end{bmatrix} \tag{2.17a}$$

$$\begin{bmatrix}(1+\lambda)\sin(1-\lambda)\gamma & -\sin(1+\lambda)\gamma\\ -(1-\lambda)\cos(1-\lambda)\gamma & \cos(1+\lambda)\gamma\end{bmatrix}\begin{pmatrix}a_2\\ b_2\end{pmatrix} = \begin{bmatrix}0\\ 0\end{bmatrix} \tag{2.17b}$$

where $\gamma$ is the specific coordinate in correspondence of the notch free border, where boundary conditions are applied (see figure2.4 ). By solving the systems in (2.17) one would find two eigenproblems, represented by equations 2.18, through which the eigenvalues relative to mode I and II fracture can be calculated.

$$\lambda\sin(2\gamma) + \sin(2\lambda\gamma) = 0 \tag{2.18a}$$

$$\lambda\sin(2\gamma) - \sin(2\lambda\gamma) = 0 \tag{2.18b}$$

The solution of these problem for sharp V-notches is due to William (who however did not use the more general complex analysis proposed by Muskhelishvili), that in 1952 was able to provide the eigenvalues $\lambda_1$ (mode

I) and $\lambda_2$ (mode II) and therefore define the stress field singularity degree for mode I and II in function of the notch opening angle ($2\alpha$) as previously illustrated in figure 2.5.

By considering the equations constituting the system defined in (2.17) is possible to expressed coefficient $b_1$ and $b_2$ in function of $a_1$ and $a_2$ respectively:

$$b_1 = (1-\lambda_1)\chi_1 a_1 \qquad b_2 = (1+\lambda_2)\chi_2 a_2$$

where

$$\chi_1 = -\frac{\sin(1-\lambda_1)\gamma}{\sin(1+\lambda_1)\gamma} \qquad \chi_2 = -\frac{\sin(1-\lambda_2)\gamma}{\sin(1+\lambda_2)\gamma}$$

In addition, by focusing on the notch bisector (i.e. $\theta = 0$), and remembering the definitions in (2.5) and (2.6) coefficient $a_1$ and $a_2$ can be related to the more useful $K_1$ and $K_2$ previously defined:

$$a_1 = \frac{K_1}{\sqrt{2\pi}\lambda_1[(1+\lambda_1)+\chi_1(1-\lambda_1)]} \tag{2.19a}$$

$$a_2 = -\frac{K_2}{\sqrt{2\pi}\lambda_2[(1-\lambda_2)+\chi_1(1+\lambda_2)]} \tag{2.19b}$$

Hence, by substituting equations (2.19) in (2.15) and (2.16), after the aforesaid assumptions and simplifications, the final expressions for the stress field are:

$$\begin{pmatrix} \sigma_{\theta\theta} \\ \sigma_{rr} \\ \tau_{r\theta} \end{pmatrix}_I = \frac{r^{\lambda_1-1}K_1}{\sqrt{2\pi}(1+\lambda_1)+\chi_1(1-\lambda_1)} \left[ \begin{pmatrix} (1+\lambda)\cos(1-\lambda)\theta \\ (3-\lambda)\cos(1-\lambda)\theta \\ (1-\lambda)\sin(1-\lambda)\theta \end{pmatrix} + b_1 \begin{pmatrix} \cos(1+\lambda)\theta \\ -\cos(1+\lambda)\theta \\ \sin(1+\lambda)\theta \end{pmatrix} \right] \tag{2.20}$$

$$\begin{pmatrix} \sigma_{\theta\theta} \\ \sigma_{rr} \\ \tau_{r\theta} \end{pmatrix}_{II} = \frac{r^{\lambda_2-1}K_2}{\sqrt{2\pi}(1-\lambda_2)+\chi_1(1+\lambda_2)} \left[ \begin{pmatrix} -(1+\lambda)\sin(1-\lambda)\theta \\ -(3-\lambda)\sin(1-\lambda)\theta \\ +(1-\lambda)\cos(1-\lambda)\theta \end{pmatrix} + b_2 \begin{pmatrix} \sin(1+\lambda)\theta \\ -\sin(1+\lambda)\theta \\ -\cos(1+\lambda)\theta \end{pmatrix} \right] \tag{2.21}$$

where subscript $I$ and $II$ refer to mode I and II stress components respectively.

## 2.5 Mode III - Antiplane loading condition

Muskhelishvili's method is valid only for in-plane problems, and can not be applied to the out-of-plane case of mode III loading. However, in the last years, a solution for the problem of torsion of notched shaft has been presented by Lazzarin and Zappalorto [26] by means of the theory of complex numbers. Specifically, a holomorphic function $H(z)$ was introduced , whose form has to be defined from case to case depending on the relevant boundary conditions.

We avoid here to treat the whole formulation and we present the solution for the case of cracked shaft under torsion:

$$\begin{pmatrix} \tau_{zr} \\ \tau_{z\varphi} \end{pmatrix} = \frac{K_3}{\sqrt{2\pi r}} \begin{pmatrix} \sin(\frac{\varphi}{2}) \\ \cos(\frac{\varphi}{2}) \end{pmatrix} \tag{2.22}$$

were the adopted polar coordinate system $(r, \varphi)$ can be seen in figure 2.6.

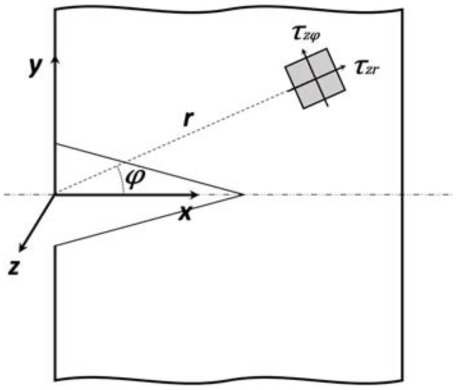

Figure 2.6: Polar coordinate system $(r, \varphi)$ centered at the crack tip.

# Chapter 3

# Strain Energy Density

For many years the Strain Energy Density (SED) has been used to formulate failure criteria for materials exhibiting both ductile and brittle behavior. Since Beltrami [27] to nowadays the SED has been found being a powerful tool to assess the static and fatigue behavior of notched and unnotched components in structural engineering. Different SED-based approaches were formulated by many researchers and applied both to static and fatigue loading conditions [28, 29, 30].

This chapter present all the mathematical derivation required to formulate the Averaged Strain Energy Density (ASED) criterion, which is the method widely used in this work to study the failure of materials.

Starting from definition of SED, important formulas are derived by means of the equations obtained in the previous chapter for in-plane problem, which will eventually establish the basis for ASED method. First, the problem of components weakened by sharp V-notches is treated, followed by the more complex case of blunt V-notches. Finally, at the end of the chapter, an extension of ASED for mode III fracture is presented.

## 3.1 ASED: a volume-based approach

The ASED method as formalized by Lazzarin and Zambardi [17] for sharp notches and by Lazzarin and Berto for blunt notches [18], is reminiscent of Neuber's concept of elementary volume, according to which the failure of metallic components is determined by the averaged stress in a control volume rather than the peak stress at the notch tip [19].

It is a method that condenses together the advantages to be an energy based criterion with those tied to the definition to a material-dependent structural volume.

The SED approach is based on the idea that, under prevailing tensile stresses, failure occurs when the strain energy density averaged over a given control volume ($\overline{W}$) reaches a critical value, $W_c$, where $W_c$ depends on the material.

The total strain energy density for an isotropic material obeying a linear elastic law is:

$$W(1,2) = \frac{1}{2E}[\sigma_{11}^2+\sigma_{22}^2+\sigma_{33}^2-2\nu(\sigma_{11}\sigma_{22}+\sigma_{11}\sigma_{33}+\sigma_{22}\sigma_{33})+2(1+\nu)\sigma_{12}^2] \quad (3.1)$$

where $E$ and $\nu$ represents the elastic modulus and the Poisson's ratio respectively and subscripts $1, 2, 3$ refer to the stress components in a given reference coordinate system.

## 3.2 In-plane loading conditions

In the following subsections the ASED method is presented for plane problems, starting with the case of components weakened by sharp v-notches and successively with blunt v-notches. The stress analysis carried out in the previous chapter is now useful to formalize ASED criterion for mode I and II fracture.

### 3.2.1 Sharp V-notches

In the case of a sharp V-shaped notch, the symmetric (mode I) and the skew symmetric (mode II) stress distribution are defined by equations (2.20) and (2.21) respectively. By considering for the moment a general three-axial problem and taking advantage of the superposition principle, we can express the total stress field in the vicinity of the notch tip as follow:

$$\sigma_{ij}(r,\theta) = r^{\lambda_1-1}K_1 \begin{bmatrix} \tilde{\sigma}_{\theta\theta}^{(1)} & \tilde{\sigma}_{r\theta}^{(1)} & 0 \\ \tilde{\sigma}_{r\theta}^{(1)} & \tilde{\sigma}_{rr}^{(1)} & 0 \\ 0 & 0 & \tilde{\sigma}_{zz}^{(1)} \end{bmatrix} + r^{\lambda_2-1}K_2 \begin{bmatrix} \tilde{\sigma}_{\theta\theta}^{(2)} & \tilde{\sigma}_{r\theta}^{(2)} & 0 \\ \tilde{\sigma}_{r\theta}^{(2)} & \tilde{\sigma}_{rr}^{(2)} & 0 \\ 0 & 0 & \tilde{\sigma}_{zz}^{(2)} \end{bmatrix} \quad (3.2)$$

where now $\sigma_{ij}$ represents a generic component of stress, and the angular stress functions $\tilde{\sigma}_{\theta\theta}$ , $\tilde{\sigma}_{rr}$ and $\tilde{\sigma}_{r\theta}$ for Mode I (superscript 1) and for Mode II (superscript 2) are expressed in closed form through equations (2.20) and (2.21).

By substituting into (3.1) the explicit expressions for stresses (3.2), one obtains for the total strain energy density ($W$)

$$W(r,\theta) = W_1(r,\theta) + W_2(r,\theta) + W_{12}(r,\theta) \tag{3.3}$$

where

$$\begin{aligned} W_1(r,\theta) =& \frac{1}{2E} r^{2(\lambda_1-1)} K_1^2 [\tilde{\sigma}_{\theta\theta}^{(1)^2} + \tilde{\sigma}_{rr}^{(1)^2} + \tilde{\sigma}_{zz}^{(1)^2} + \\ & - 2\nu(\tilde{\sigma}_{\theta\theta}^{(1)}\tilde{\sigma}_{rr}^{(1)} + \tilde{\sigma}_{\theta\theta}^{(1)}\tilde{\sigma}_{zz}^{(1)} + \tilde{\sigma}_{rr}^{(1)}\tilde{\sigma}_{zz}^{(1)}) + 2(1+\nu)\tilde{\sigma}_{r\theta}^{(1)^2}] \end{aligned} \tag{3.4a}$$

$$\begin{aligned} W_2(r,\theta) =& \frac{1}{2E} r^{2(\lambda_2-1)} K_2^2 [\tilde{\sigma}_{\theta\theta}^{(2)^2} + \tilde{\sigma}_{rr}^{(2)^2} + \tilde{\sigma}_{zz}^{(2)^2} + \\ & - 2\nu(\tilde{\sigma}_{\theta\theta}^{(2)}\tilde{\sigma}_{rr}^{(2)} + \tilde{\sigma}_{\theta\theta}^{(2)}\tilde{\sigma}_{zz}^{(2)} + \tilde{\sigma}_{rr}^{(2)}\tilde{\sigma}_{zz}^{(2)}) + 2(1+\nu)\tilde{\sigma}_{r\theta}^{(2)^2}] \end{aligned} \tag{3.4b}$$

$$\begin{aligned} W_{12}(r,\theta) =& \frac{1}{E} r^{(\lambda_1+\lambda_2-2)} K_1 K_2 + [\tilde{\sigma}_{\theta\theta}^{(1)}\tilde{\sigma}_{\theta\theta}^{(2)} + \tilde{\sigma}_{rr}^{(1)}\tilde{\sigma}_{rr}^{(2)} + \tilde{\sigma}_{zz}^{(1)}\tilde{\sigma}_{zz}^{(2)} + \\ & - \nu(\tilde{\sigma}_{\theta\theta}^{(1)}\tilde{\sigma}_{rr}^{(2)} + \tilde{\sigma}_{\theta\theta}^{(1)}\tilde{\sigma}_{zz}^{(2)} + \tilde{\sigma}_{rr}^{(1)}\tilde{\sigma}_{\theta\theta}^{(2)} + \tilde{\sigma}_{rr}^{(1)}\tilde{\sigma}_{zz}^{(2)} + \\ & + \tilde{\sigma}_{zz}^{(1)}\tilde{\sigma}_{\theta\theta}^{(2)} + \tilde{\sigma}_{zz}^{(1)}\tilde{\sigma}_{rr}^{(2)}) + 2(1+\nu)\tilde{\sigma}_{r\theta}^{(1)}\tilde{\sigma}_{r\theta}^{(2)}] \end{aligned} \tag{3.4c}$$

The elastic deformation energy in a region of radius $R$ around the notch tip is calculated as the integral of the strain energy density $W$ in the volume. However, as we are now considering a plane problem, the theory does not lose validity if the integral is carried out in a respective control area, as follow:

$$E(R) = \int_0^R \int_{-\gamma}^{+\gamma} [W_1(r,\theta) + W_2(r,\theta) + W_{12}(r,\theta)] r \, dr \, d\theta \tag{3.5}$$

where the meaning of the angular coordinate $\gamma$ can be deduced in figure 2.4. Since the integration field is symmetric with respect to the notch bisector, the contribution of $W_{12}$ vanishes. As a consequence:

$$E(R) = E_1(R) + E_2(R) = \frac{I_1(\gamma)}{4E\lambda_1} K_1^2 R^{2\lambda_1} + \frac{I_2(\gamma)}{4E\lambda_2} K_2^2 R^{2\lambda_2} \tag{3.6}$$

where $I_1$ and $I_2$ represent the integral of the angular function for mode I and II respectively:

$$
\begin{aligned}
I_1(\gamma) = \int_{-\gamma}^{\gamma} & (\tilde{\sigma}_{\theta\theta}^{(1)^2} + \tilde{\sigma}_{rr}^{(1)^2} + \tilde{\sigma}_{zz}^{(1)^2} - 2\nu(\tilde{\sigma}_{\theta\theta}^{(1)}\tilde{\sigma}_{rr}^{(1)} + \tilde{\sigma}_{\theta\theta}^{(1)}\tilde{\sigma}_{zz}^{(1)} + \tilde{\sigma}_{rr}^{(1)}\tilde{\sigma}_{zz}^{(1)}) + \\
& + 2(1+\nu)\tilde{\sigma}_{r\theta}^{(1)^2}) \, d\theta
\end{aligned}
\tag{3.7a}
$$

$$
\begin{aligned}
I_2(\gamma) = \int_{-\gamma}^{\gamma} & (\tilde{\sigma}_{\theta\theta}^{(2)^2} + \tilde{\sigma}_{rr}^{(2)^2} + \tilde{\sigma}_{zz}^{(2)^2} - 2\nu(\tilde{\sigma}_{\theta\theta}^{(2)}\tilde{\sigma}_{rr}^{(2)} + \tilde{\sigma}_{\theta\theta}^{(2)}\tilde{\sigma}_{zz}^{(2)} + \tilde{\sigma}_{rr}^{(2)}\tilde{\sigma}_{zz}^{(2)}) \\
& + 2(1+\nu)\tilde{\sigma}_{r\theta}^{(2)^2}) \, d\theta
\end{aligned}
\tag{3.7b}
$$

We remind here that plane stress conditions occur when $\sigma_{zz} = 0$ while plane strain condition result when $\sigma_{zz} = \nu(\sigma_{\theta\theta} + \sigma_{rr})$ . The area on which the integration is carried out is:

$$
A(R) = \int_0^{R_0} \int_{-\gamma}^{+\gamma} r \, dr \, d\theta = R_0^2 \gamma \tag{3.8}
$$

where $R_0$ is the control radius (that will be defined and discussed in the next section) and $\gamma$ the angle between the notch flank ant the notch bisector being given in radians.

Therefore, the elastic deformation energy, averaged on the area $A$, is defined as:

$$
\overline{W} = \frac{E(R)}{A(R)} = \frac{e_1}{E} K_1^2 R_0^{2(\lambda_1 - 1)} + \frac{e_2}{E} K_2^2 R_0^{2(\lambda_2 - 1)} \tag{3.9}
$$

where

$$
e_1(2\alpha) = \frac{I_1(\gamma)}{4\lambda_1\gamma} \qquad e_2(2\alpha) = \frac{I_2(\gamma)}{4\lambda_2\gamma}
$$

Values of $e_1$ and $e_2$ are already provided in the contributions by Lazzarin et al.[17, 18] as a function of the notch opening angle $2\alpha$.

We have already seen in the previous section that, according to ASED method, failure occurs when the strain energy density averaged over a given control volume reaches a critical value, $W_c$ , where $W_c$ and the control volume are thought to be properties of the material.

If the material behavior is ideally brittle, then $W_c$ can be evaluated by using simply the conventional ultimate tensile strength $\sigma_t$, so that

$$
W_c = \frac{1}{2E} \sigma_t^2 \tag{3.10}
$$

In principle, $W_c$ as determined from uniaxial tests cannot be considered independent on the loading mode. Under compression or torsion, for example, the critical value of $W_c$ may be different from the critical value under tension.

In plane problems, (i.e. mode I, mode II or mixed, I and II), considering the case of cracks or sharp V-notches, the control volume becomes a circle or a circular sector with a radius $R_0$ centered in the notched tip as illustrated in figure 3.1a and 3.1b.

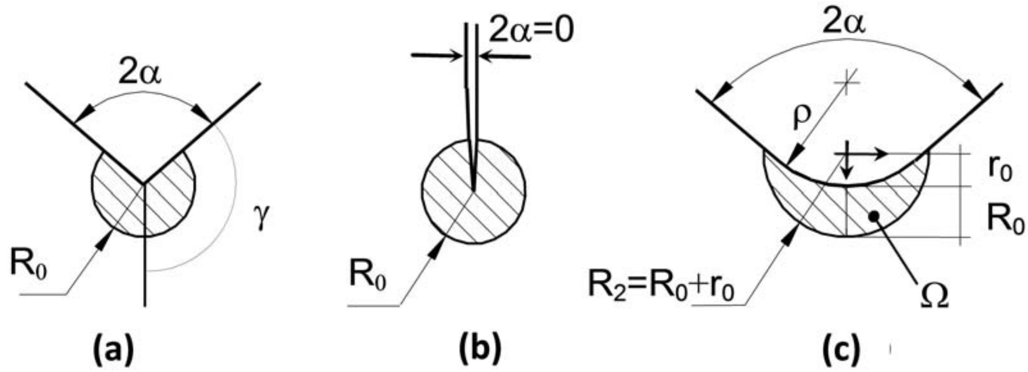

Figure 3.1: Critical volume (area) for sharp V-notch (a), crack (b) and blunt V-notch (c). Distance $r_0 = \rho\frac{\pi-2\alpha}{2\pi-2\alpha}$.

Assuming now negligible the mode II contribution of averaged strain energy in (3.9), one obtains

$$\overline{W} = \frac{E(R)}{A(R)} = \frac{e_1}{E}K_1^2 R_0^{2(\lambda_1-1)} \tag{3.11}$$

It is now evident that, at failure conditions ($\overline{W} = W_c$), $K_1$ is equal to the critical value of notch stress intensity factor $K_{1c}$ ($K_{Ic}$ for the particular case of crack), which is a property of the material. Therefore, remembering (3.10) and solving equation (3.11) for $R_0$:

$$R_0 = \left(\sqrt{2e_1}\frac{K_{1c}}{\sigma_t}\right)^{\frac{1}{1-\lambda_1}} \tag{3.12}$$

Values of $\lambda$ and integration parameter $e_1$ are already provided in several contributions by Lazzarin et al. [17, 18] here reported in table 3.1.

| $2\alpha$ | $\gamma$[rad] | $\lambda_1$ | $\lambda_2$ | $\lambda_3$ | $e_1$ | $e_2$ | $e_3$ |
|---|---|---|---|---|---|---|---|
| 0 | $\pi$ | 0.5 | 0.5 | 0.5 | 0.13449 | 0.34139 | 0.4138 |
| $\pi/6$ | $11\pi/12$ | 0.5014 | 0.5982 | 0.5455 | 0.14485 | 0.27297 | 0.37929 |
| $\pi/3$ | $5\pi/6$ | 0.5122 | 0.7309 | 0.6 | 0.15038 | 0.2153 | 0.34484 |
| $\pi/2$ | $3\pi/4$ | 0.5445 | 0.9085 | 0.6667 | 0.14623 | 0.16793 | 0.31034 |
| $2\pi/3$ | $2\pi/3$ | 0.6157 | 1.1489 | 0.75 | 0.12964 | 0.12922 | 0.27587 |
| $3\pi/4$ | $5\pi/8$ | 0.6736 | 1.3021 | 0.8 | 0.11721 | 0.1125 | 0.25863 |

Table 3.1: Values of parameters in equation 3.15 valid for materials obeying a linear elastic law and with Poisson's ratio $\nu = 0.3$.

A useful expression for the radius $R_0$ defining the control volume has been provided for the crack case under plane strain conditions [32]:

$$R_0 = \frac{(1+\nu)(5-8\nu)}{4\pi}\left(\frac{K_{IC}}{\sigma_t}\right)^2 \tag{3.13}$$

The results provided by equation (3.13) matches those provided by equation (3.12).

### 3.2.2 Blunt V-notches

In the case of blunt notches, where the tip is characterized by a notch tip radius $\rho$ different from zero, the area that controls the fracture according to ASED criterion assumes a crescent shape. Here, $R_0$ is the maximum width assumed by such a crescent shape area measured along the notch bisector line (see figure 3.1c).

The distance $r_0$ in figure 3.1c is calculated by the following expression [18]:

$$r_0 = \rho\frac{\pi - 2\alpha}{2\pi - 2\alpha}$$

and the control radius $R_2$ for the case of blunt notches becomes, according to figure 3.1c

$$R_2 = R_0 + r_0 \tag{3.14}$$

Interestingly, under in-plane mixed-mode loading, the control area is no longer centered with respect to the notch bisector, but rigidly rotated with respect to it and centered on the point where the SED (and the maximum principal stress) reaches its maximum value [33].

This rotation is shown in figure 3.2 where the control area is drawn for a U-shaped notch both under mode I loading (figure 3.2a) and mixed-mode loading (figure 3.2b).

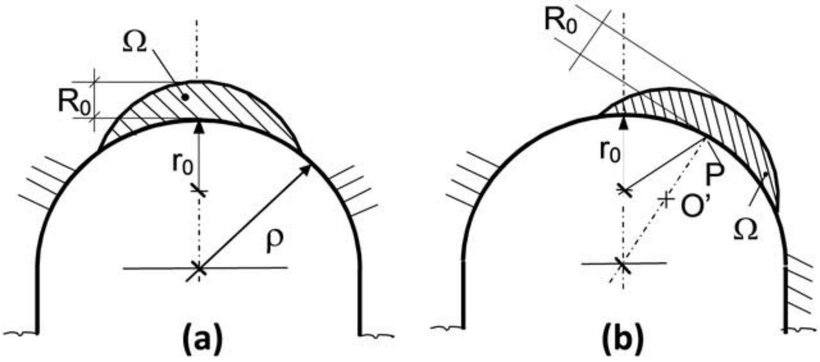

Figure 3.2: Critical volume for U-notch under mode I (a) and mixed mode loading (b).

## 3.3 Out-of-plane loading conditions

While equation (3.9) can be used to study all the case of pure mode I, mode II and mix mode I and II fracture, dealing with mode III fracture, the formulation has to be updated to assess the cases where mode I, II and III conditions are combined together.

Taking again advantage of the superposition principle, hence adding the contribution tied to mode III, the expression for the strain energy density can be modified as follows:

$$\overline{W} = \frac{e_1}{E} K_1^2 R_0^{2(\lambda_1 - 1)} + \frac{e_2}{E} K_2^2 R_0^{2(\lambda_2 - 1)} + \frac{e_3}{E} K_3^2 R_0^{2(\lambda_3 - 1)} \tag{3.15}$$

where $e_3$ is listed in Lazzarin's papers [17, 18], under Beltrami hypothesis, and here reported in table 3.1 for the Poisson's ratio $\nu = 0.3$. In addition, $K_3$ is the mode III notch stress intensity factor already defined in (2.7).

# Chapter 4

# Finite elements analysis

The study of fracture and notch mechanics has been strongly encouraged over the last decades by the development of sophisticated software dedicated to finite elements (FE) analysis. For instance, at the state of the art, there is no available analytical expression to calculate stress intensity factors, which are therefore obtained exclusively by numerical methods.

In this chapter, the implementation of finite element method trough the commercial software ANSYS (release 16.2) is described in detail, to carry out both bi- and tri-dimensional structural analysis.

The purpose of such analysis can be summarize as follow:

- Implement iterative analysis to explore the fracture behavior of a large number of cases with different specimen geometries and mixed mode loading.

- Obtain the relevant stress intensity factors.

- Give a prediction of the failure load by means of an averaged strain energy density (ASED) criterion.

All the different type of specimens employed in this work are presented here, discussing their geometrical features in function of the mode fracture investigation, and their numerical implementation. At the beginning, the modelling of two-dimensional problem is presented, useful for the assessment of in-plane fracture mode. Successively, cases of tridimensional problems with mixed mode I and III loading conditions are discussed. Particular attention is given to describe a novel numerical procedure to apply ASED criterion to mixed mode I and III fracture by means of numerical analysis.

## 4.1 2D-Analysis

Two-dimensional models were useful to simulate the case of in-plane loading, namely the case of mixed mode I-II. The experimental configurations considered in this work were

- Four Point Bending (FPB) specimen
- Flattened V-notch Semi Disk (FVSD)
- Round-tip V-notched Brazilian Disk (RVBD)

APDL codes were implemented for every case in order to easily parameterize the problem, permitting an iterative investigation of different geometries and load conditions.

Considering the large value of thickness versus other dimensions, the entire set of specimens was assumed to be under plane strain conditions. The 8-node biquadratic plane strain quadrilateral elements (solid plane183) were used to mesh different FE models.

Moreover, when dealing with cracks, the singular elements (quadratic elements with the midside nodes placed at the quarter points) were employed for the first ring of elements around the crack tip. In ANSYS the singular element was created by defining a so-called *Concentration Key Point*.

The great advantage of such elements, together with the creation of a fine mesh, was to reveal the high gradient of the stress field near the crack tip, and therefore to give more accurate results regarding the evaluation of stress intensity factors (SIFs).

Materials were modelled as perfect elastic and isotropic, hence by simply defining Young modulus $E$ and Poisson's ratio $\nu$.

A quite large number of experimental data are used in this work as a comparison with numerical analysis, hence, different materials, ranging from ceramics, polymers and metals, were considered. However, all the materials were assume to undergo brittle or quasi-brittle fracture, in accordance with the hypothesis of linear elasticity required by ASED method.

All the materials properties obtained from literature and used in the FE modeling and ASED calculation, are resumed in the next chapter, when discussing the results of FE analysis.

According to the procedure provided in reference [34], the fracture loads of FPB specimens were estimated under mixed mode loading condition using Average Strain Energy Density criterion (ASED).

The fracture parameter $K_{IC}$, together with ultimate strength $\sigma_t$ of the material under consideration were defined to calculate the value of control radius $R_0$ and critical strain energy density $W_c$ by means of equation (3.13) and (3.10) respectively.

However, in the case of FVSD specimens a different approach for the definition of $R_0$ and $W_c$ was required, and the procedure will be discussed in the appropriate section (4.1.2).

A unit external load ($F$) was applied to FE models in order to obtain the mean value of strain energy density ($\overline{W}$) in the control volume previously defined.

According with ASED criterion, failure occurs when strain energy density averaged in a volume around the notch tip reaches the critical value$W_c$ depending on materials properties as shown in equation (3.10).

Therefore, taking advantage of the linearity of the problem, the value of failure load predicted by numerical analysis ($F_{FEM}$) was obtain by the following simple proportion between the unitary applied load $F$ and the square root of $\overline{W}$ :

$$\frac{F_{FEM}}{F} = \sqrt{\frac{W_c}{\overline{W}}} = F_{FEM} \tag{4.1}$$

### 4.1.1 Four point Bending

A cracked four-point bend (FPB) specimen with dimensions of $L \times W \times T$ and initial crack length $a$ was considered for fracture analysis with linear elastic behavior assumption.

Figure 4.1 illustrates the specimen geometrical parameters, where $S_0$ is a variable parameter representing the offset between the crack and the midpoint of the specimen.

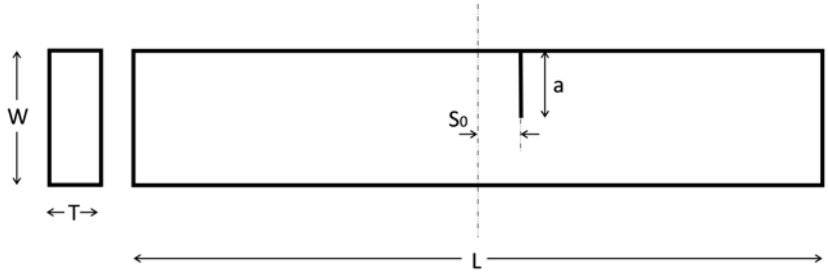

Figure 4.1: Cracked four-point bend (FPB) specimen showing dimensions $L \times W \times T$, initial crack length $a$ and geometrical parameter $S_0$.

As illustrated in figure 4.2, a typical mesh of the FPB specimen presented higher density near the crack tip, in order to improve the accuracy of the results.

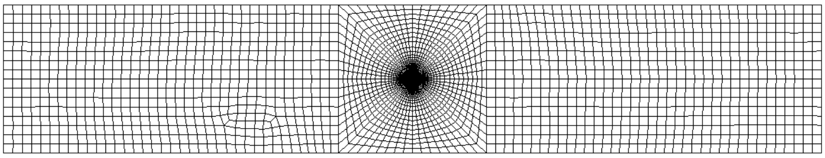

Figure 4.2: Typical mesh pattern for FE model of FPB specimen showing the adopted high density mesh near the crack tip.

Figure 4.3a and b show the geometry and loading arrangement for anti-symmetric four point and symmetric four point bending specimens respectively, together with the corresponding applied loads, shear force and bending moment diagrams.

Taking into consideration the case of anti-symmetric four point bending specimen (figure 4.3a), given that the bending moment, $M$, is associated with mode I, and that the shear force, $Q$, is related to mode II, it is clear that the ratio between the fracture mode I and mode II components varies with the position of the crack relative to the loading point (hence by varying the distance $S_0$).

Specifically, along the center axis of the loading arrangement $M$ is equal to zero, yet there is a substantial $Q$. Therefore, a crack positioned exactly on the central axis is loaded in pure mode II.

If the crack is positioned away from the center, $Q$ remains constant while $M$ expands, and therefore the mode I to mode II ratio increases.

Pure mode I is obtained from symmetric four point bending tests (figure 4.3b) by positioning the crack in the central region where $Q = 0$, and therefore where there is no mode II contribution.

Pure mode I was considered under symmetric conditions (i.e. $L1 = L2$, $L3 = L4$ and offset $S_0 = 0$) while pure mode II tests were considered under anti-symmetric four point bend loading (i.e. $L1 = L4$, $L2 = L3$ and offset $S_0 = 0$).

Different mode mixities can be provided by either considering constant values of $L1 = L4$ and increasing $L3$ from $L2$ toward the crack location, or by varying the offset $S_0$, i.e. moving the crack along the specimen with respect to the loading fixture. Different models with varying $L3$ or $S_0$ were created according to the procedure adopted in the experimental set-up described in literature.

The mode mixity was investigated using the elastic mix mode index, $Me$, defined as follow:

$$Me = \frac{2}{\pi}\arctan\Big(\frac{K_I}{K_{II}}\Big) \tag{4.2}$$

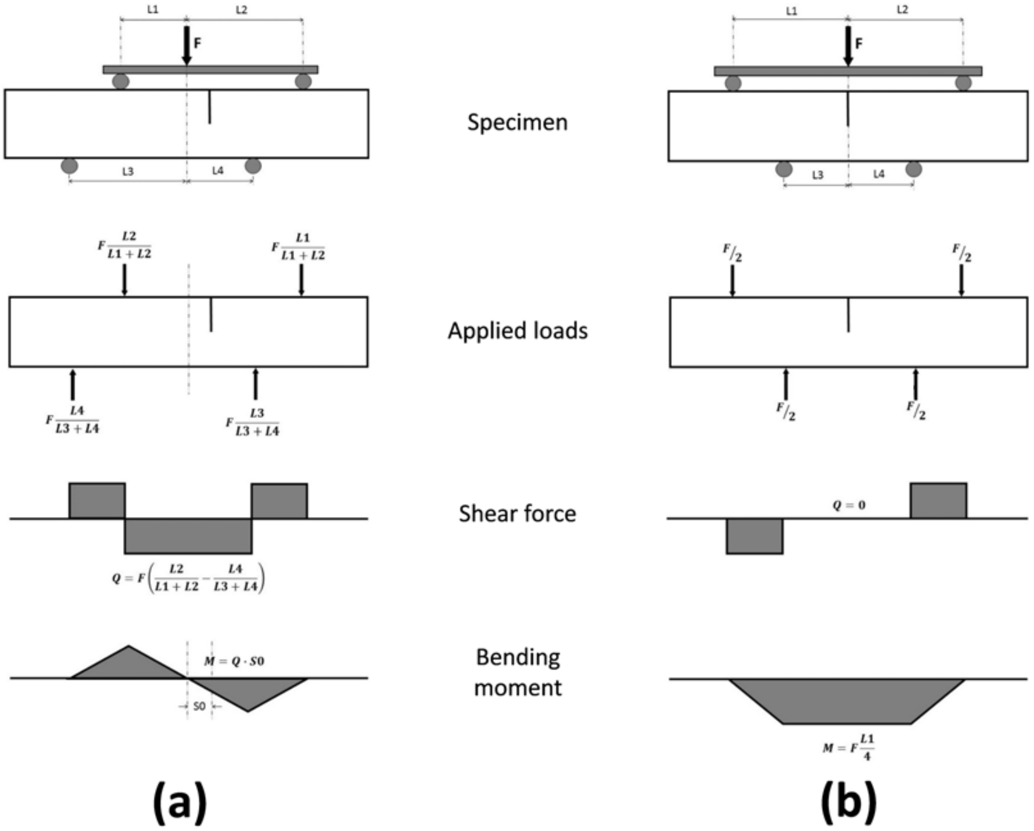

Figure 4.3: Geometry, loading arrangement, applied loads, shear force and bending moment diagrams for anti-symmetric (a) four point and symmetric (b) four point bending specimens.

Different length ratios of $\frac{L3}{L1}$ were considered for different mixed mode loading conditions which corresponds to the elastic mixity parameter ($Me$) ranging from 0 (pure mode II) to 1 (pure mode I).

A quite large number of materials are investigated in this thesis for the case of FPB specimens, that will be presented and discussed separately in the next chapter.

### 4.1.2 Flattened V-notch Semi-Disk

The so-called Flattened V-notch Semi-Disk (FVSD) is a novel specimen proposed by Torabi et al. [35] useful for performing compressive fracture tests on V-notches, hence without any case of mix loading conditions. FVSD specimen is schematically represented in figure 4.4.

The parameters $2\alpha, \rho, a, b, L, t$ and $P$ are the notch angle, the notch ra-

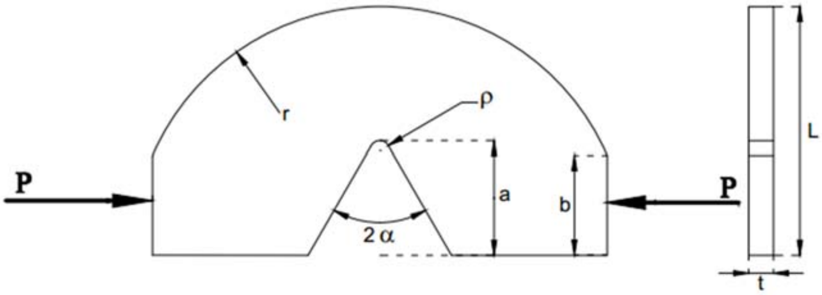

Figure 4.4: Scheme of FVSD specimen with geometrical parameters $L, t, a, b, \rho, 2\alpha$, and applied load $P$.

dius, the notch length, the flattened length, the disk radius, the specimen thickness and the remotely applied compressive load respectively.

In particular, the case of interest is a blunt V-notch, therefore with a notch radius different from zero.

Taking advantage of the symmetry of the problem, only half of the specimen was modeled. Figure 4.5 illustrates, as an example, the typical mesh of the model for the case of $a = 10\,\mathrm{mm}$, $\rho = 0.5\,\mathrm{mm}$ and $2\alpha = 30\,°$, where a total of 543 elements were employed.

Minimum element size was set to 0.2 mm, in order to model the curve shape of the notch tip radius, rather than to achieve numerical convergence, given that ASED method does not require very fine mesh (since it does not involve the derivative of displacements).

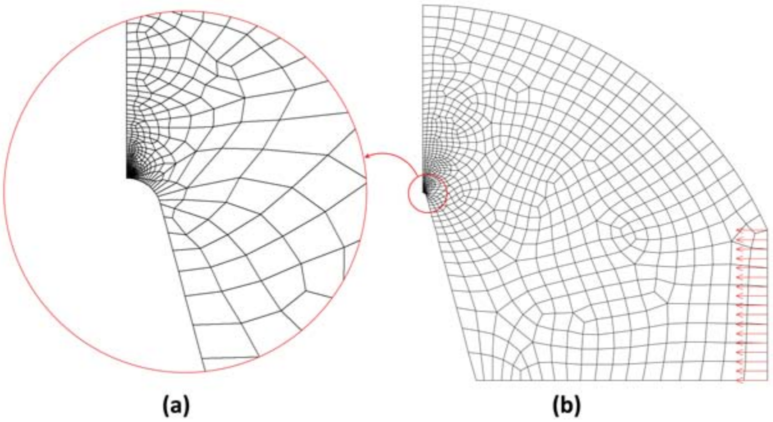

Figure 4.5: Typical mesh (b) of FVSD specimen for the case of $a = 10\,\mathrm{mm}$, $\rho = 0.5\,\mathrm{mm}$ and $2\alpha = 30\,°$ with focus on the notch tip (a).

As in the case of FPB specimen, discussed in the previous section, a numerical APDL code was implemented with the aim of parametrize geometrical dimensions $a$, $\rho$ and $2\alpha$, to allow an iterative investigation of all the experimental data.

### 4.1.3 Round-tip V-notch Brazilian Disk

Round-tip V-notch Brazilian Disk (RVBD) is a specimen frequently utilized in brittle fracture tests of blunt V-notches [36, 37, 38]. Recently, Torabi et al. [39] used this specimen to investigated mixed mode I and II fracture with negative mode I contribution, hence by applying a compressive load, which will be studied in this work by means of numerical analysis.

The material employed in [39] and modeled in finite elements is polymethyl methacrylate (PMMA), which is assumed here to present perfect linear elastic behavior. The geometry of RVBD is schematically illustrated in figure 4.6.

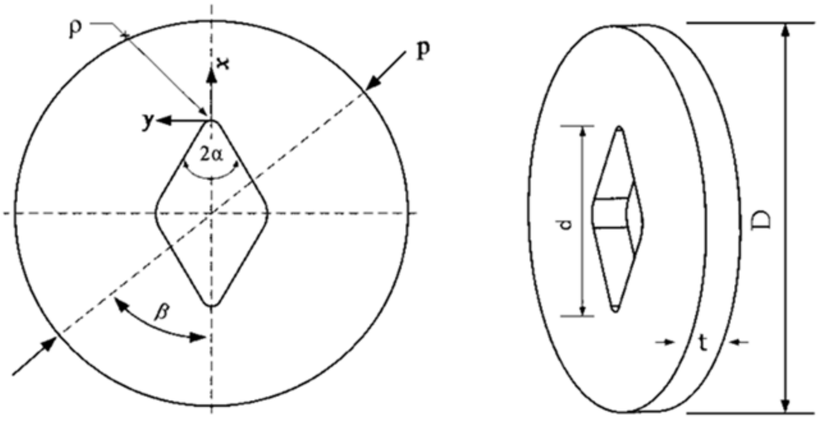

Figure 4.6: Scheme of RVBD specimen with geometrical parameters $D, d, t, \rho, 2\alpha, \beta$ and applied compressive load $P$.

The parameters $2\alpha, \rho, t, d, D$ and $P$ are the notch opening angle, the notch tip radius, the disk thickness, twice the notch length (i.e. the overall slit length), the disk diameter and the applied compressive load, respectively. The disk diameter, the overall slit length and the disk thickness are considered to be constant and equal to 80 mm, 40 mm and 8 mm, respectively.

Different notch angles and notch radii were considered by implementing an APDL code that iteratively investigated different geometries. The values considered in this work are the following: $2\alpha = 30^\circ$ and $60^\circ$ and $\rho = 0.5$ , 1, 2 and 4 mm.

Angle $\beta$, represented in figure 4.6, is the angle between the notch bisector line and the applied load direction, and it was set as an iterative parameter.

A typical mesh of the RVBD specimen is depicted in figure 4.7 for the case of $2\alpha = 30\,^\circ$, $\rho = 1\,\mathrm{mm}$ and loading angle $\beta = 30\,^\circ$, where a total number of 5602 elements were used.

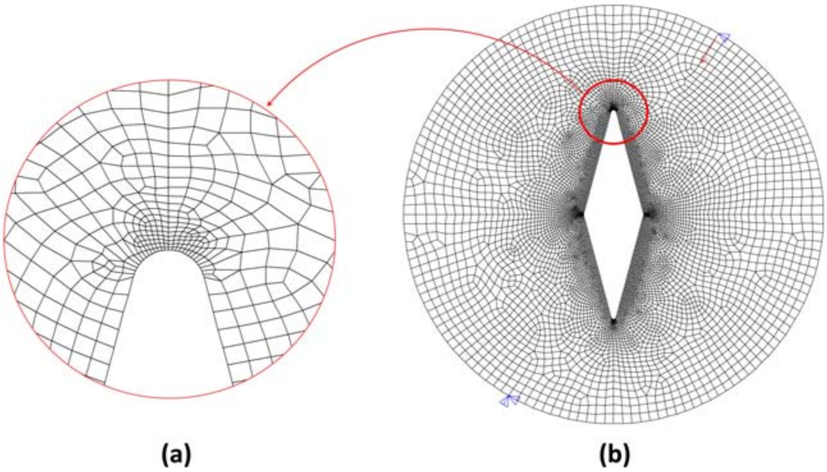

Figure 4.7: Typical mesh for RVBD specimen (b) with $2\alpha = 30\,^\circ$, $\rho = 1\,\mathrm{mm}$ and loading angle $\beta = 30\,^\circ$. Figure (a) shows an enlargement of the mesh at the notch tip.

Pure positive mode I loading condition at the main V-shaped corners of the slit is achieved when $\beta = 0$. With increasing values of $\beta$, the mode fracture varies from pure mode I to pure mode II, and eventually, at the specific angle named $\beta_{II}$, pure mode II loading is obtained. According to [37], $\beta_{II}$ is always less than $90\,^\circ$ and varies in function of the notch opening angle, the notch length and the notch tip radius. By increasing values of $\beta$ beyond $\beta_{II}$, the fracture mode presents a greater and greater negative mode I contribution up to the limit case of $\beta = 90\,^\circ$, where pure compressive mode I loading is achieved.

In summary, for $0\,^\circ < \beta < \beta_{II}$ the notch experiences mixed mode I and II under positive mode I conditions, while for $\beta_{II} < \beta < 90\,^\circ$ under negative ones.

In reference [39] the value of $\beta_{II}$ for different notch radii is determined to be between $26\,^\circ$ and $27\,^\circ$ for $2\alpha = 30\,^\circ$ and between $28\,^\circ$ and $30\,^\circ$ for $2\alpha = 60\,^\circ$, for various notch tip radii. It is also important to note that at a certain value of $\beta$ between $\beta_{II}$ and $90\,^\circ$, named critical loading angle $\beta_c$, the fracture does not occur anymore at the main V-notch corner.

The finite element (FE) analyses have revealed that for $2\alpha = 30\,^\circ$ and $60\,^\circ$, $\beta_c$ values are in the range of $55\,^\circ$ to $60\,^\circ$ and $50\,^\circ$ to $55\,^\circ$, respectively. Thus, several appropriate values of $\beta$ between $\beta_{II}$ and $\beta_c$ (i.e. $\beta = 30\,^\circ$, $40\,^\circ$

and 50 ° for $2\alpha = 30\,°$ and $\beta = 30\,°$, 40 ° and 45 ° for $2\alpha = 60\,°$) have been selected for performing mixed mode I and II brittle fracture tests on the main V-notches under negative mode I conditions.

An important observation, useful for the correct modeling of ASED criterion to the case of RVBD specimen, is now proposed. Experimental evidence showed that fracture occurred at the right half border of the round V-notch. In reference [39], it has been illustrated that the right half border experienced tensile tangential stresses during loading while the notch bisector line and the left half border of the notch sustained compressive stresses.

The main conclusion is that although the RVBD specimens have been tested under combined compressive-shear loading conditions, brittle fracture still initiates from the right half border of the round V-notch due to the local tensile stresses.

As a consequence, despite the applied compressive load, control radius was defined according to equation (3.13), valid for tensile conditions. The position of the control volume is found by the method already presented in section 3.2.2, hence centered where the maximum principal stress occurred.

The following numerical procedure was iterated for different geometrical and loading parameters in an APDL code:

- A model describing a RVBD specimen with defined geometric and loading parameters was first solved by applying a unit load. Maximum principal stress at the notch tip, and consequently the position of control volume, were evaluated.
- Elements constituting the control volume were created and a new solution was obtained with the same loading conditions.
- ASED calculation was carried out and critical failure load was derived by means of the proportion already discussed at the beginning of this chapter.

## 4.2 3D-Analysis

In order to investigate the case of mixed mode I-III a bi-dimensional model was no more useful, as long as the out of plane component could not be revealed. Therefore, creation of 3D models was required.

The case of interest was a cracked specimen loaded with a particular fixture proposed for the first time by Ayatollahi and Saboori [40]. The system is schematically represented in figure 4.8a, while the specimen is shown in figure 4.8b.

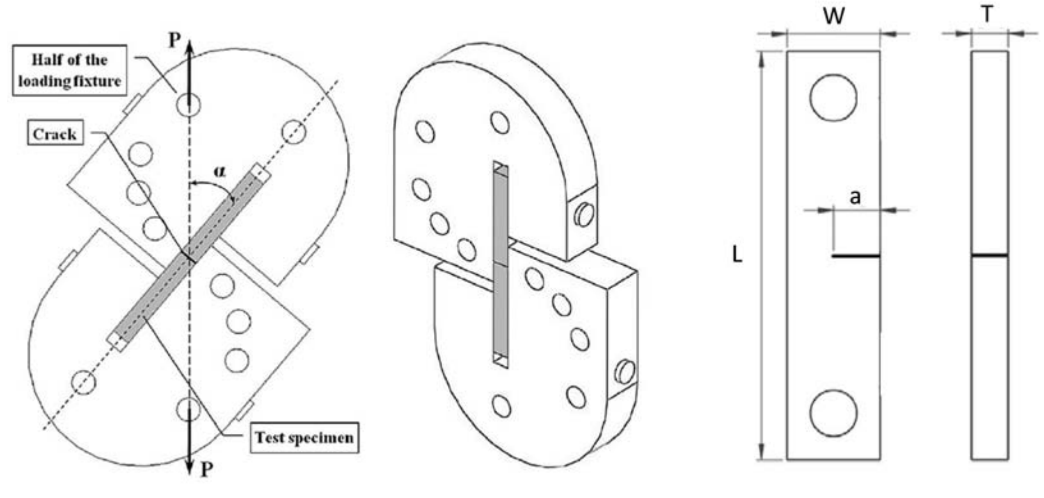

(a) (b)

Figure 4.8: Scheme of the experimental fixture introduced by Ayatollahi and Saboori [40] (a) and the cracked specimen with dimensions $L \times W \times T$ (b).

The main advantage introduced by the experimental apparatus proposed by Ayatollahi and Saboori was the possibility to carry out tests from pure mode I to pure mode III with the use of a simple tensile machine, hence avoiding time-consuming and expensive multiaxial test machines.

In fact, depending on the magnitude of the angle $\alpha$ defined in figure 4.8, pure mode I ($\alpha = 0\,^\circ$), pure mode III ($\alpha = 90\,^\circ$) and three mixed mode loading cases ($\alpha = 40\,^\circ$, $65\,^\circ$ and $78\,^\circ$) were investigated.

Since the loading fixture and the connecting bolts were made from a high strength steel alloy, they were much stiffer than the specimen, and therefore were modeled in FE analysis as rigid bodies (i.e. with a material of extremely high elastic modulus $E$).

Differently from the case of two-dimensional analysis, here the modeling of both the experimental fixture and the specimen involved the numerical implementation of contact conditions between the outer surfaces of the connection bolts and the inner surfaces of the bolt-holes made in the specimen.

In addition, a distinct contact condition was modeled between the side faces of the specimen which came in contact with the fixture during mode III loading. The contact interactions of the mentioned surfaces were defined using the *Pair-based Contact* approach already available in ANSYS 16.2.

The main idea of this approach was to identify the two surfaces defining the contact as a *target* and a *contact* surface respectively. In our case, the faces of the fixture, being much stiffer than the PMMA specimen, were modeled as *target* surfaces, while the areas of the specimen were defined as *contact* ones.

Hence, ANSYS assigned,through the auto-meshing tools *ESURF* a new typology of elements to the meshed surfaces: target170 and contact174 as *target* and *contact* elements respectively.

Each loading mode was modeled by applying a unit load to the fixture at the corresponding loading holes while constraining the symmetrical one. In order to simulate the real experimental conditions, all the degrees of freedom (DOFs) of the constrained hole were set to zero. Also the DOFs of the loaded hole, except for its load-line displacement, were constrained.

Both the specimen and the fixture were modeled by extrusion of 8-node biquadratic elements (plane183) into 20-node brick elements (solid186).

The meshed model of the specimen is simply made by extrusion of the plane elements employed in two-dimensional analysis and is represented in figure 4.9.

As already seen for the two dimensional specimen, very fine elements were utilized close to the crack tip in order to reveal the high stress gradient ahead the crack. In addition, in order to obtain more accurate results, singular elements with the middle nodes at quarter-point positions were used near the crack.

The mesh of the whole loading configuration consisting of the specimen, the fixture and the bolts is illustrated in figure 4.10.

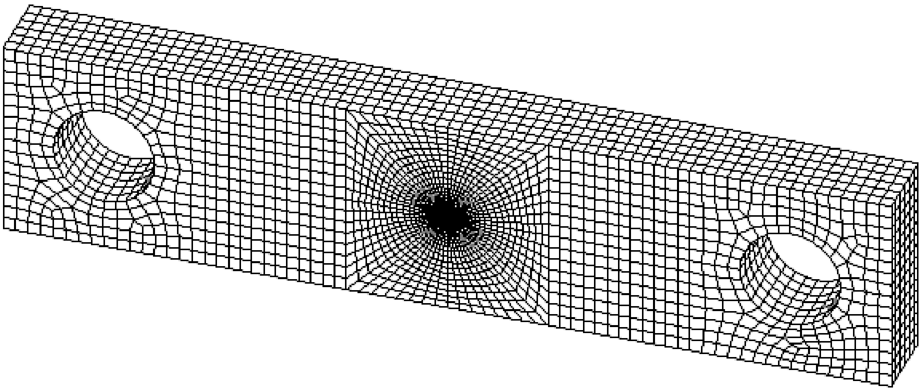

Figure 4.9: Three-dimensional mesh of the cracked specimen tested under mixed mode I and III loading conditions.

Some important observations have to be considered in the case of mixed mode I and III fracture regarding the material properties.

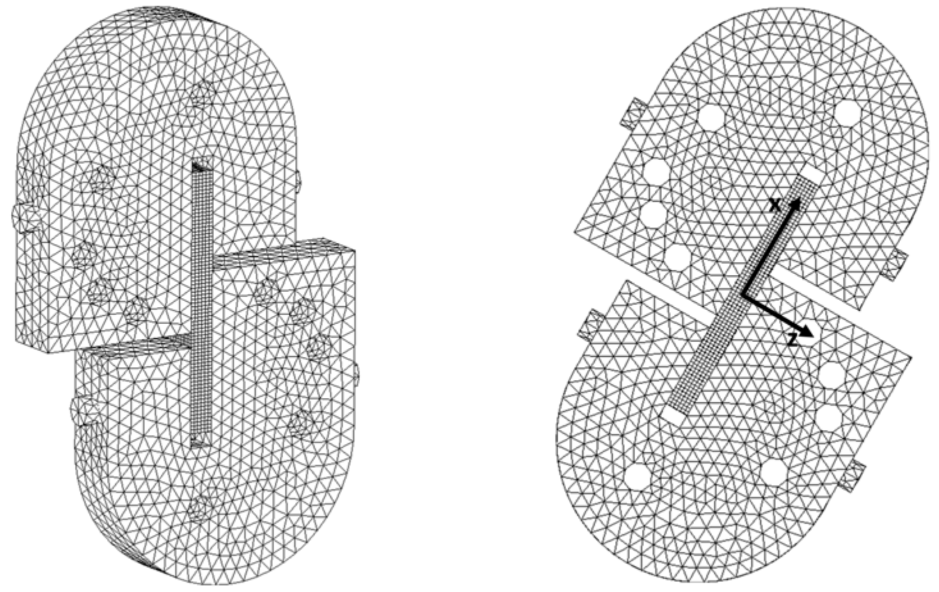

Figure 4.10: Three-dimensional mesh of the experimental system for mix mode I and III investigation

In reference [41], under uniaxial loading, the behavior showed by the tested PMMA specimen was the typical one of a brittle material: the load vs. displacement curve was linear up to the complete failure. On the contrary, the material behavior showed by the notched specimens loaded in torsion was seen to be much more complex. In particular, the torque vs. angle curves were characterized by an initial linear-elastic stretch followed by an almost horizontal plateau preceding the final fracture.

Finally, under combined tension-torsion the material cracking behavior was seen to be in between the two extreme conditions discussed above.

Further experimental investigations were made by Berto et al. [42]: under torsion load, a number of nonlinear elastic effects were detected resulting in a control volume dependent on the loading mode. The radius of the volume under torsion resulted to be much greater than the radius under tensile loading.

A non-conventional approach, based on the 'apparent' linear elastic SED evaluated considering a different critical radius, allowed to overcome the problems tied to different fracture mechanisms occurring under mode I and mode III loading and summarize the main body of the data under torsion loading in a quite narrow scatterband.

It is the author's opinion that a similar plastic phenomena due to out of plane loads, such the case of torsion, occurred in the specimens tested by

Ayatollahi and Saboori in [40].

Therefore, taking inspiration from the above observations and the studies in [42], in this work, the problem of dealing with large scale plasticity occurring at the crack tip while using a linear analysis has been overcome by considering an 'apparent' value of SED, averaged in a control volume whose dimensions vary from pure mode I to pure mode III.

In this sense, the term 'apparent' seemed to be appropriate to describe the SED value measured without any clear distinction between non-linear intrinsic and extrinsic mechanisms and based on a linear-elastic analysis of the stress distribution on the highly stressed zone ahead of the notch tip.

Hence, being conscious that a synthesis based on the apparent value of the linear elastic SED is only an engineering tool for strength assessments, SED method has been applied in this work to the data from out of plane loads, despite the presence of large scale yielding.

As a first attempt, preliminary analysis were made in this thesis to apply SED method for the case under consideration with the hypothesis of linear elasticity and constant control radius (with the same procedure used in the case of 2D analysis).

However the remarkable discrepancy between prediction results and experimental data found as a first result, particularly with increasing component of mode III fracture, encouraged the hypothesis of large scale yielding at the crack tip discussed above.

Therefore, the following considerations were proposed to extend SED method to out of plane cases.

The first assumption for the evaluation of an 'apparent' SED was to consider a value of critical strain energy density $W_c$ independent from the mode of fracture. Specifically, $W_c$ was calculated by means of equation (3.10).

The next step was the definition of a control radius variable from mode I to mode III. In this work, the following procedure was adopted: considering equations (3.12) or (3.13), was possible, for the case of pure mode I, to calculate a control radius $R_{0,I}$, in the same way as in two-dimensional analysis already discussed.

Then, considering equation (3.15) in the case of crack ($\lambda_3 = 0.5$), with pure mode III and critical conditions ($\overline{W} = W_c$ and $K_3 = K_{IIIc}$ ), under the assumption of constant $W_c$, was possible to write the following

$$W_c = \frac{e_3}{E R_{0,III}} K_{IIIc}^2 \tag{4.3}$$

By solving equation (4.3) for $R_{0,III}$, one obtains

$$R_{0,III} = \frac{e_3}{EW_c} K_{IIIc}^2 \tag{4.4}$$

The idea was to average the strain energy density in a volume whose dimensions increase from the case of pure mode I to the case of pure mode III.

The problem was then to deal the intermediate cases of mixed mode I and III, where a value of control radius was not available.

The approach adopted in this work consisted in the separation of the problem in two contributions, one for mode I and the other for mode III. The following numerical procedure was adopted and iterated to investigate different mix mode conditions

- A model with a fixed mode mixity index (i.e. a fixed experimental configuration) was first solved by applying a unit force at the loading hole corresponding to the mode mixity case under consideration. X and Z displacements were recorded at the nodes constituting the loading hole in the fixture.

- The same experimental case was than solved by using the same constraints as in the previous solution, but applying the recorded X displacement to the nodes at the loading hole, instead of a force. ASED calculations were carried out by using a critical volume defined by $R_{0,I}$ to obtain a first contribution of SED, namely $SED_1$, were subscript 1 refers to the components of strain energy density related to mode I fracture.

- Another model was solved in the same way as described in the previous point but applying the detected Z displacement. Strain energy was than averaged in a volume defined by $R_{0,III}$ and the contribution of mode III fracture, $SED_3$, was obtained.

- The total strain energy density ($\overline{W}$) was derived by adding the mode I and III components
$$\overline{W} = SED_1 + SED_3 \tag{4.5}$$

- Finally, prediction of the critical load ($F_{FEM}$) was done by means of the proportion in equation (4.1).

The idea of the procedure describe above, was to face the separation of mode I and III contribution by applying separated X and Z displacements, where displacements in X are thought to be related to mode I fracture while displacements in Z are supposed to be associated with mode III fracture.

It is worthwhile to observe that, in principle, the separated application of displacements in X and Z direction does not correspond to a superposition effect: a correct superposition principle could have been proposed if one has decomposed the applied unit force into X and Z components, hence solving the corresponding two different scenarios.

However, a method consisting in the decomposition of the applied load into two components, clearly does not allow the distinct analysis of mode I and III contributions, since the loading in the X or Z direction would equally result into a mixed mode case.

Furthermore, the simple adding of energy contributions as shown in equation (4.5) is, from a physical point of view, incorrect: in a general case, the total deformation energy due to the simultaneous application of two forces (or two displacements) is not equal to the sum of energy as if the forces (or displacements) would have been applied separately. There is also a mutual component of work that needs to be taken into account, which does not appear in equation (4.5) (that however deal with strain energy density averaged in different volumes, instead of strain energy).

Therefore, the proposed idea does not refer to a superposition principle and does not account for a correct energy summation. However we re-mark that the method has to be thought as an engineering tool to assess the fracture of components loaded under mixed mode I and III conditions, rather than to answer to a real physical phenomenon.

# Chapter 5

# Results and discussion

In this chapter all the results obtained for the fracture assessment are presented and discussed. Fracture assessment is done exclusively by applying ASED criterion, as explained in the previous chapter.

First bi-dimensional analysis regarding plane problem of mixed mode I and II are considered. At the beginning relevant outcomes of finite elements analysis relative to four point bending (FPB) tests are presented providing an overview of application of ASED method for different classes of isotropic materials (i.e. ceramics, polymers and metals).

Successively, results concerning the negative mode I (FVSD specimen) and mixed compressive mode I and II (RVBD specimen) are listed and commented.

At the end of the chapter, three-dimensional analysis of mixed mode I and III are exhibited and discussed.

## 5.1 FPB specimen

As explained in section (4.1.1), a number of different experimental data are analyzed here by means of numerical analysis with ASED method. In the case of the FPB specimen, results related to ceramics, polymers and metals are presented separately.

### 5.1.1 Ceramic materials

The material properties relative to the ceramics considered in this work are displayed in table 5.1.

| | GR | BGR | MA | KK | SWT | WPD | ALU | SLG |
|---|---|---|---|---|---|---|---|---|
| $E$(GPa) | 45 | 82 | 35 | 36.7 | 78.08 | 69.6 | 348 | 73.3 |
| $\nu$ | 0.28 | 0.21 | 0.27 | 0.21 | 0.21 | 0.285 | 0.23 | 0.23 |
| $\sigma_t$(MPa) | 12.2 | 16.7 | 7.95 | 7.62 | 10.4 | 15.11 | 261 | 76.9 |
| $K_{IC}$(MPam$^{0.5}$) | 1.393 | 2.148 | 1.386 | 0.6227 | 1.198 | 0.4176 | 4.4 | 0.62 |
| Reference | | [43] | | [44] | [44] | [44] | [45] | [45] |

Table 5.1: Material properties of the investigated materials: Granite (GR), Black Granite (BGR), Marble (MA), Kristallina of Kavala (KK), Snow White of Thassos (SWT), White of Piges Drama (WPD), Alumina (ALU) and Soda-Lime Glass (SLG).

The set of materials included six different samples of rocks (two type of granites and four typologies of marble), Alumina, and Glass as explained in caption of table 5.1.

As explained in the previous chapter, ASED calculation was made by selecting the elements inside the control volume and numerically evaluating the strain energy density (SED).

Figure 5.1, relative to the case of Granite (GR), shows the elements in the surrounding of the crack tip and the typical strain energy contours. One can notice the different shape of plastic zone revealed by finite element analysis occurring at the crack tip varying from pure mode I ($Me = 1$) to pure mode II ($Me = 0$).

In every model, Stress Intensity factors (SIFs) were derived through the *CINT* tool, a method for the calculation of SIFs already implemented in ANSYS software, that involves the definition of a contour integral path in analogy with the J-integral method mentioned in chapter 1.

Substituting the material properties in table 5.1 and the values of stress intensity factors $K_1$ and $K_2$ derived from numerical analysis into equation (3.9), one is able to analytically calculate a value of strain energy density related to the unit load applied.

By using this value of strain energy and the proportion shown in equation (4.1) a fracture load value ($F_{an}$) can be obtained.

By substituting the values of fracture parameters $K_1$ and $K_2$ into equation (4.2) the correspondent mix mode index $Me$ was calculated. Hence, the value of the strain energy density (SED) relative to unit load was obtained and used to calculated the predictive failure load, as explained in the previous chapter.

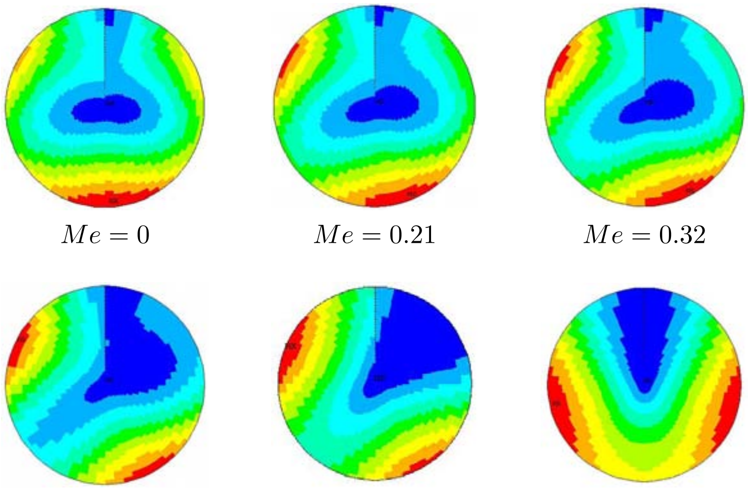

$Me = 0$ $Me = 0.21$ $Me = 0.32$

$Me = 0.51$ $Me = 0.70$ $Me = 1$

Figure 5.1: The typical strain energy contours in the control volume of FPB specimens for different mixity mode parameter $Me$.

Numerical value of plane strain fracture toughness $K_{Ic}$ and $K_{IIc}$ are obtained respectively by taking the value of $K_1$ and $K_2$ correspondent to the case of pure mode I ($Me = 1$) and II ($Me = 0$) multiplied for the relative critical load calculated by numerical ASED prediction (hence taking advantage of the linear elasticity of the model).

Tables from 5.2 to 5.9 collect, for different materials, the relevant data obtained from finite elements models including mix mode parameter $Me$, critical SIFs $K_{Ic}$ and $K_{IIc}$, numerical prediction load ($F_{FEM}$) and the value of prediction load calculated analytically ($F_{an}$). For all the materials, except Alumina and Soda-Lime Glass, experimental failure load ($F_{exp}$) was reported in literature, and also added in table from 5.2 to 5.9 together with the percentage discrepancy ($\Delta\%$) between experimental and prediction load results.

The results of such prediction models are graphically illustrated in figures from 5.2 to 5.9, which represent for every investigated material the numerical and analytical failure prediction according to ASED criterion, and the experimental critical load in function of $Me$.

Results relative to Stress Intensity Factors analysis for all the considered ceramics except the types of marble studied in [44] are also illustrated in figures from 5.2 to 5.9, where the plot $K_I/K_{IC}$ vs. $K_{II}/K_{IC}$ is graphically compared to the correspondent set of data obtained experimentally.

For the cases where experimental failure load was provided, the square root of the ratio between the averaged strain energy density ($\overline{W}$), numeri-

| $Me$ | $K_{Ic}$ (MPa m$^{0.5}$) | $K_{IIc}$ (MPa m$^{0.5}$) | $F_{FEM}$ (N) | $F_{an}$ (N) | $F_{exp}$ (N) | $\Delta\%$ (%) | $\sqrt{\frac{W}{W_c}}$ |
|---|---|---|---|---|---|---|---|
| 1 | 1.516 | 0.000 | 1019 | 957 | 936 | 8.14 | 0.92 |
| 0.7 | 1.155 | 0.589 | 2743 | 2625 | 2711 | 1.16 | 0.99 |
| 0.51 | 0.786 | 0.771 | 3875 | 3786 | 3506 | 9.53 | 0.90 |
| 0.31 | 0.461 | 0.857 | 4508 | 4455 | 4555 | 1.03 | 1.01 |
| 0.23 | 0.328 | 0.878 | 4692 | 4650 | 4970 | 5.93 | 1.06 |
| 0.21 | 0.305 | 0.881 | 4720 | 4680 | 4695 | 0.53 | 0.99 |
| 0 | 0.040 | 0.899 | 4954 | 4925 | 4480 | 9.58 | 0.90 |

Table 5.2: Fracture parameters and failure load prediction for Granite (GR).

cally obtained by applying the correspondent experimental failure load, and $W_c$, has been calculated. The square root ratio between $\overline{W}$ and $W_c$ is listed in tables from 5.2 to 5.9 for different type of investigated ceramics and summarized in figure 5.10. In addition, the cases of Glass (SLG) and Alumina (ALU) were included in figure 5.10 deriving a value of averaged strain energy density $\overline{W}$ by substituting experimental values of $K_1$ and $K_2$ in equation (3.9).

In the case of Granite (GR), there is a very good agreement between experimental and numerical data for pure mode I, pure mode II and all the investigated mixed mode I and II.

Results are displayed in figure 5.2, where the excellent matching between calculated stress intensity factors, $K_{Ic}$ and$K_{IIc}$, and the ones reported in literature [] is illustrated. The obtained value of fracture toughness $K_{Ic}$ is 1.516 MPam$^{0.5}$, as shown in table 5.2 for the case of pure mode I fracture, which is comparable with the value of 1.393 MPam$^{0.5}$ reported in literature, and in very good agreement with the one obtained from tested GR specimens.

Numerical analysis relative to Black Granite (BGR) seemed to simulate correctly the experimental trend of failure load. However, in the case of pure mode II ($Me = 0$), a large discrepancy (almost 200% ) was found between the averaged value of experimental failure load and FE model.

As shown in figure 5.3, in the case of pure mode II, a quite large scattering of experimental results was reported with respect to the other investigated mixed modes, where data arranged in a very narrow scatter band. However, the minimum value for the failure of BGR specimens is about 2 KN, which

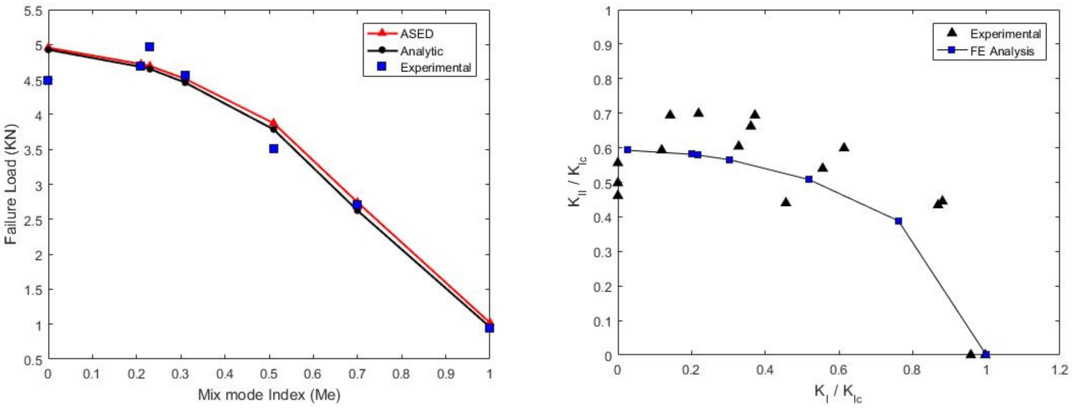

Figure 5.2: Failure prediction and SIFs analysis of Granite (GR).

is remarkably higher than the value predicted by the FE model. Therefore, such huge difference could be ascribed to some large scale yielding phenomena that might occur with increasing mode II component.

The failure of the prediction model for the mixed mode towards pure mode II fracture, is depicted also by SIFs analysis, showing that the discrepancy between empirical and numerical data increases with increasing mode II. However, the value of plain strain fracture toughness obtained from finite elements analysis, equal to 2.403 $\mathrm{MPam}^{0.5}$ was in good agreement with the value of 2.148 $\mathrm{MPam}^{0.5}$ mentioned in literature.

Predictions regarding the case of Marble (MA) were quite satisfactory, as illustrated in figure 5.4. However, discrepancy for both pure mode I and II is above 50%, where in the case of pure mode I the predicted load is above the empirical one (which turned in a less safety assessment of failure).

An overview of the statistical nature of the reported data would be necessary here to allow a better comparison of data.

As in the case of BGR specimens, the SIFs analysis for MA provided consistent results only for pure mode I fracture, while there was an overall underestimation of SIFs moving toward pure mode II.

The experimental set-up for the typology of marble tested by Xeidakis et al. [44] turned out to address a quite narrow range of ratio between mode I and II fracture, since the smallest value found for mix mode parameter $Me$ was equal to 0.86. Nevertheless, numerical analysis successfully evaluate the fracture for the different investigated materials.

In the case of Kristallina of Kavala (KK) only one case ($Me = 0.93$) seems to be unsuccessfully predicted by the FE model, presenting a discrepancy

| $Me$ | $K_{Ic}$<br>(MPa m$^{0.5}$) | $K_{IIc}$<br>(MPa m$^{0.5}$) | $F_{FEM}$<br>(KN) | $F_{an}$<br>(KN) | $F_{exp}$<br>(KN) | $\Delta\%$<br>(%) | $\sqrt{\frac{W}{W_c}}$ |
|---|---|---|---|---|---|---|---|
| 1 | 2.403 | 0.001 | 2.063 | 2.011 | 2.071 | 0.38 | 1.02 |
| 0.62 | 1.564 | 1.058 | 7.097 | 7.228 | 7.505 | 5.75 | 1.07 |
| 0.52 | 1.255 | 1.178 | 7.496 | 7.775 | 8.027 | 7.08 | 1.04 |
| 0.38 | 0.875 | 1.276 | 7.798 | 8.250 | 8.637 | 10.76 | 1.08 |
| 0.3 | 0.662 | 1.313 | 7.881 | 8.411 | 9.287 | 17.83 | 1.16 |
| 0.2 | 0.437 | 1.34 | 7.904 | 8.493 | 9.841 | 24.52 | 1.24 |
| 0.1 | 0.207 | 1.354 | 7.857 | 8.490 | 23.116 | 194.21 | 3.09 |

Table 5.3: Fracture parameters and failure load prediction for Black Granite (BGR).

higher than 45%. However, one would note that according to experimental evidence, the case of $Me = 0.93$ seems to be less critical than the case of $Me = 0.92$, where the component of mode I fracture is lower. This is unlikely to be true in reality, since the opening mode of fracture is well known to be the most critical among the others. The trend of experimental failure can be justifying by the slightly variation of mix mode index $Me$, meaning that the results are likely to be subjected to experimental inaccuracies.

Satisfactory results were obtained in the cases of Snow White of Thassos (SWT) and White of Piges Drama (WPD), represented in figures 5.6 and 5.7 respectively.

As already mentioned before, no data regarding failure load for Alumina (ALU) and Soda-Lime Glass (SLG) were available in literature. However, SIFs analysis from FE method, represented in figures 5.8 and 5.9, show a good compliancy with experimental data, meaning that the failure load obtained by numerical analysis for the two tested materials could be reliable.

In particular, in the case of ALU, the numerical curve $K_I/K_{Ic}$ vs. $K_{II}/K_{Ic}$ stood above the experimental results, which resulted in a slightly underestimated failure prediction. From an engineering point of view, this fact turns into a more safety design of structures, since the real failure of materials seems to occur at more critical conditions than the ones predicted by ASED method.

Finally, one of the most remarkable results of this section, is shown in

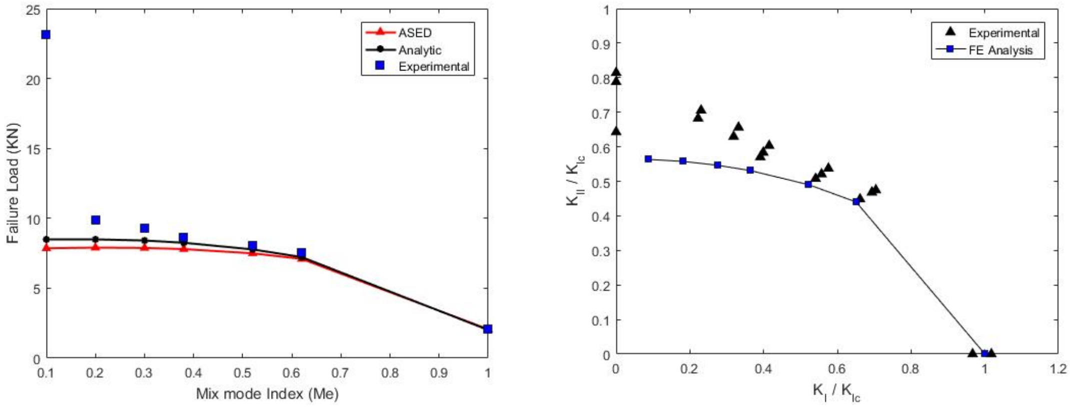

Figure 5.3: Failure prediction and SIFs analysis of Black Granite (BGR).

figure 5.10, where the square root ratio between averaged strain energy $\overline{W}$ (calculated for different sets of materials as explained in the previous chapter) and the critical strain energy density $W_c$, is graphically illustrated in function of $Me$.

The majority of the tested ceramic materials fell inside a relatively narrow scatter band ranging from 0.8 to 1.2, supporting the idea that SED is effectively a parameter that successfully describes the fracture phenomenon of the considered brittle materials.

A deeper analysis of figure 5.10 revealed that for intermediate mix mode index the entire set of experimental data were inside the scatter band, except for the case of ALU, which fell at higher value. This fact confirms that ASED method applied for the considered experimental data provided an underestimated value of failure load. At low $Me$, toward pure mode II conditions, some data regarding MA and BGR samples fell above the scatter band, and generally very few materials were below the unit value, validating the hypothesis that plasticity phenomena might have occurred with increasing component of mode II fracture.

Therefore, although all the materials treated in this study were assumed to have an ideal fragile behavior, a large-scale plasticity phenomenon could arise under different loading conditions, which could be the starting point of future investigations.

| $Me$ | $K_{Ic}$ (MPa m$^{0.5}$) | $K_{IIc}$ (MPa m$^{0.5}$) | $F_{FEM}$ (N) | $F_{an}$ (N) | $F_{exp}$ (N) | $\Delta\%$ (%) | $\sqrt{\frac{W}{W_c}}$ |
|---|---|---|---|---|---|---|---|
| 1.00 | 1.708 | 0.000 | 966 | 810 | 386 | 60.06 | 0.40 |
| 0.70 | 1.221 | 0.622 | 2442 | 2222 | 2193 | 10.20 | 0.88 |
| 0.62 | 1.045 | 0.701 | 2849 | 2666 | 2229 | 21.77 | 0.92 |
| 0.51 | 0.797 | 0.781 | 3309 | 3205 | 3413 | 3.12 | 1.04 |
| 0.31 | 0.457 | 0.849 | 3761 | 3772 | 3429 | 8.82 | 0.91 |
| 0.19 | 0.265 | 0.869 | 3937 | 3998 | 4187 | 6.32 | 1.18 |
| 0.03 | 0.039 | 0.879 | 4079 | 4170 | 6145 | 50.66 | 1.51 |

Table 5.4: Fracture parameters and failure load prediction for Marble (MA).

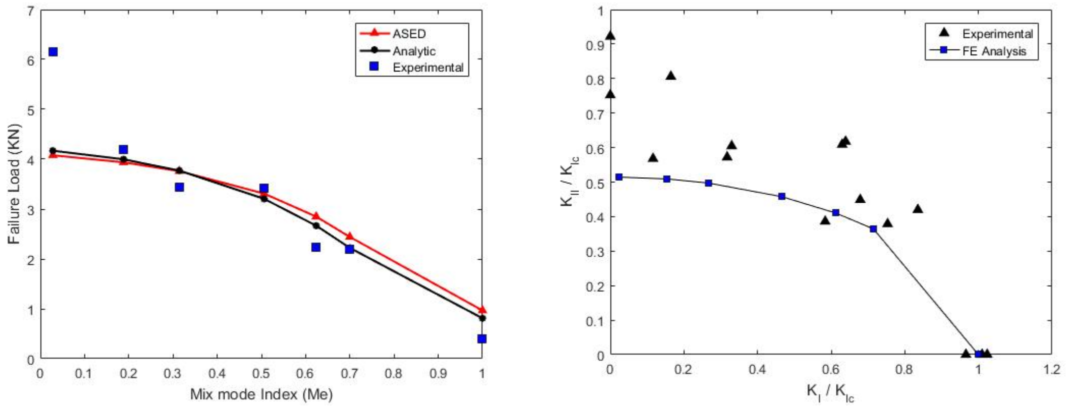

Figure 5.4: Failure prediction and SIFs analysis of Marble (MA).

| $Me$ | $K_{Ic}$ (MPa m$^{0.5}$) | $K_{IIc}$ (MPa m$^{0.5}$) | $F_{FEM}$ (N) | $F_{an}$ (N) | $F_{exp}$ (N) | $\Delta\%$ (%) | $\sqrt{\frac{W}{W_c}}$ |
|---|---|---|---|---|---|---|---|
| 0.97 | 0.652 | 0.034 | 518 | 537 | 644 | 24.43 | 1.20 |
| 0.94 | 0.647 | 0.056 | 589 | 612 | 797 | 35.19 | 1.30 |
| 0.93 | 0.643 | 0.069 | 706 | 734 | 1034 | 46.49 | 1.41 |
| 0.92 | 0.639 | 0.082 | 880 | 916 | 898 | 2.10 | 0.98 |
| 0.9 | 0.632 | 0.103 | 1154 | 1200 | | | |
| 0.86 | 0.614 | 0.141 | 1643 | 1706 | | | |

Table 5.5: Fracture parameters and failure load prediction for Kristallina of Kavala (KK).

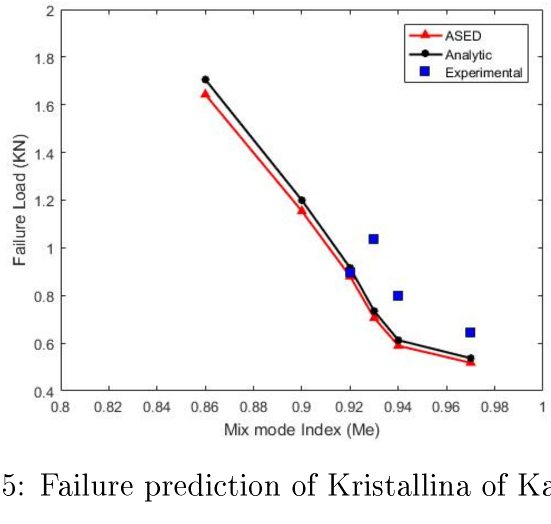

Figure 5.5: Failure prediction of Kristallina of Kavala (KK).

| $Me$ | $K_{Ic}$ (MPa $m^{0.5}$) | $K_{IIc}$ (MPa $m^{0.5}$) | $F_{FEM}$ (N) | $F_{an}$ (N) | $F_{exp}$ (N) | $\Delta\%$ (%) | $\sqrt{\frac{W}{W_c}}$ |
|---|---|---|---|---|---|---|---|
| 0.97 | 1.244 | 0.066 | 987 | 1032 | 746 | 24.41 | 0.723 |
| 0.94 | 1.233 | 0.107 | 1123 | 1178 | 881 | 21.53 | 0.748 |
| 0.93 | 1.224 | 0.132 | 1343 | 1412 | 1200 | 10.61 | 0.850 |
| 0.92 | 1.212 | 0.156 | 1669 | 1762 | 2070 | 24.02 | 1.175 |
| 0.9 | 1.193 | 0.194 | 2179 | 2309 | 2000 | 8.22 | 0.866 |
| 0.86 | 1.146 | 0.263 | 3068 | 3283 | | | |

Table 5.6: Fracture parameters and failure load prediction for Snow White of Thassos (SWT).

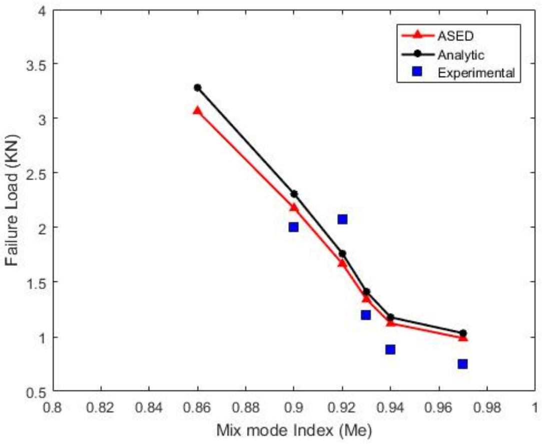

Figure 5.6: Failure prediction of Snow White of Thassos (SWT).

| $Me$ | $K_{Ic}$ (MPa m$^{0.5}$) | $K_{IIc}$ (MPa m$^{0.5}$) | $F_{FEM}$ (N) | $F_{an}$ (N) | $F_{exp}$ (N) | $\Delta\%$ (%) | $\sqrt{\frac{W}{W_c}}$ |
|---|---|---|---|---|---|---|---|
| 0.97 | 0.419 | 0.022 | 333 | 336 | 373 | 12.11 | 1.11 |
| 0.94 | 0.417 | 0.036 | 379 | 383 | 475 | 25.23 | 1.24 |
| 0.93 | 0.415 | 0.045 | 455 | 459 | 542 | 19.18 | 1.18 |
| 0.92 | 0.412 | 0.053 | 567 | 573 | 661 | 16.53 | 1.15 |
| 0.9 | 0.407 | 0.066 | 744 | 751 | 881 | 18.44 | 1.17 |
| 0.86 | 0.395 | 0.091 | 1058 | 1068 | | | |

Table 5.7: Fracture parameters and failure load prediction for White of Piges Drama (WPD).

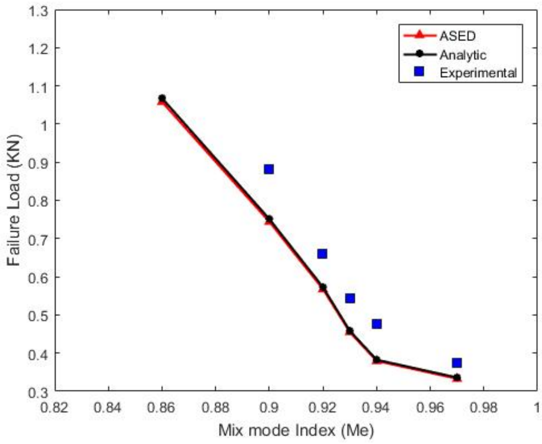

Figure 5.7: Failure prediction of White of Piges Drama (WPD).

| $Me$ | $K_{Ic}$(MPa m$^{0.5}$) | $K_{IIc}$ (MPa m$^{0.5}$) | $F_{FEM}$(N) | $F_{an}$(N) |
|---|---|---|---|---|
| 1 | 4.488 | 0 | 87 | 91 |
| 0.91 | 4.386 | 0.636 | 185 | 194 |
| 0.84 | 4.194 | 1.043 | 302 | 316 |
| 0.78 | 3.954 | 1.391 | 408 | 425 |
| 0.71 | 3.595 | 1.763 | 520 | 537 |
| 0.68 | 3.454 | 1.881 | 555 | 572 |
| 0.65 | 3.282 | 2.01 | 593 | 610 |
| 0.61 | 3.072 | 2.148 | 635 | 651 |
| 0.56 | 2.815 | 2.295 | 679 | 694 |
| 0.44 | 2.125 | 2.597 | 769 | 780 |
| 0.35 | 1.679 | 2.734 | 810 | 818 |
| 0.25 | 1.166 | 2.847 | 844 | 850 |
| 0.13 | 0.599 | 2.922 | 866 | 871 |
| 0 | 0 | 2.949 | 875 | 878 |

Table 5.8: Fracture parameters and failure load prediction for Alumina (ALU).

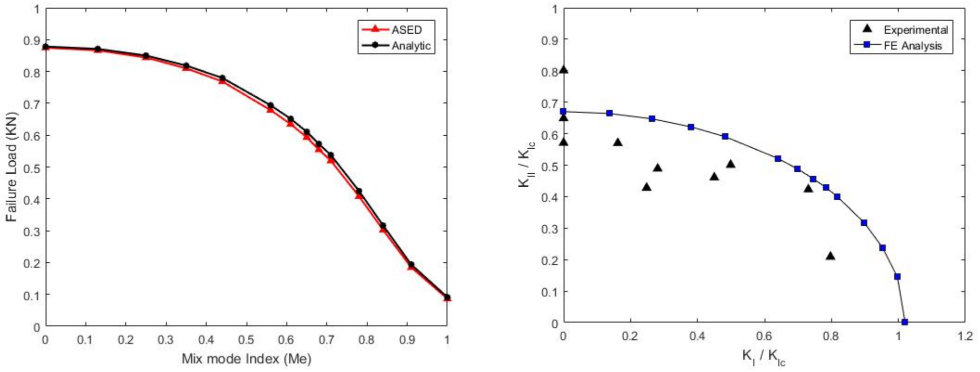

Figure 5.8: Failure prediction and SIFs analysis of Alumina (ALU).

| $Me$ | $K_{Ic}$(MPa m$^{0.5}$) | $K_{IIc}$ (MPa m$^{0.5}$) | $F_{FEM}$(N) | $F_{an}$(N) |
|---|---|---|---|---|
| 0.9 | 0.604 | 0.096 | 30 | 32 |
| 0.86 | 0.588 | 0.13 | 37 | 40 |
| 0.82 | 0.566 | 0.168 | 48 | 51 |
| 0.76 | 0.536 | 0.207 | 60 | 63 |
| 0.7 | 0.49 | 0.252 | 73 | 77 |
| 0.62 | 0.433 | 0.295 | 86 | 90 |
| 0.54 | 0.375 | 0.328 | 96 | 99 |
| 0.49 | 0.339 | 0.345 | 101 | 104 |
| 0.44 | 0.297 | 0.362 | 106 | 109 |
| 0.37 | 0.248 | 0.378 | 111 | 113 |
| 0.29 | 0.194 | 0.392 | 115 | 117 |
| 0.2 | 0.133 | 0.403 | 118 | 120 |
| 0.11 | 0.069 | 0.41 | 121 | 122 |
| 0 | 0.001 | 0.413 | 122 | 123 |

Table 5.9: Fracture parameters and failure load prediction for Soda-Lime Glass (SLG).

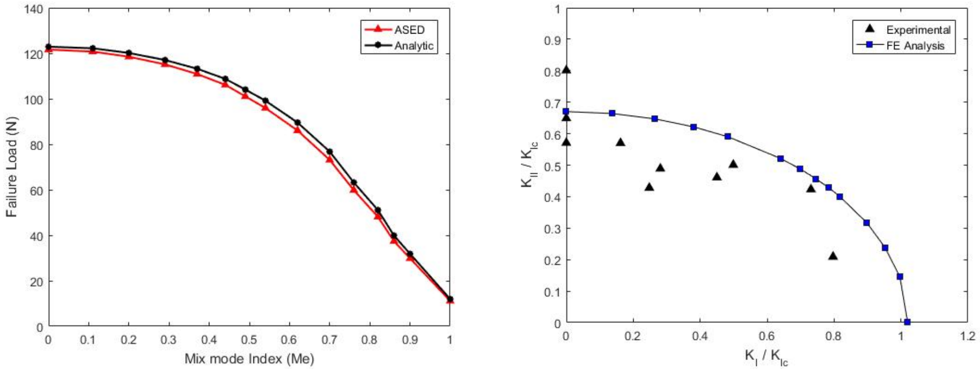

Figure 5.9: Failure prediction and SIFs analysis of Soda-Lime Glass (SLG).

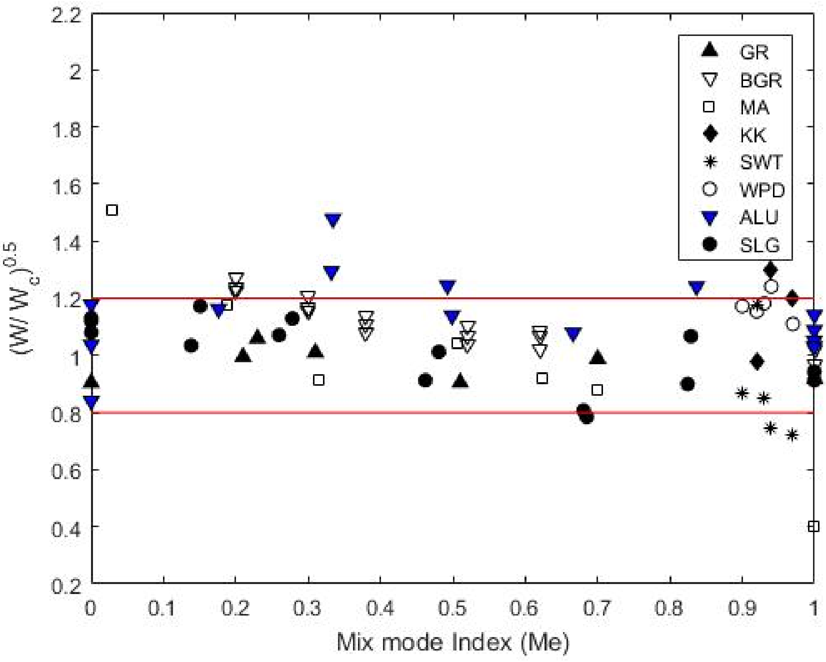

Figure 5.10: Ratio between $\overline{W}$ and $W_c$ for all the ceramic materials considered in this work.

### 5.1.2 Polymeric materials

We present here the results related to polymeric materials, Polymethyl methacrylate (PMMA) and a Polyurethane (PU) rigid foam, which properties are listed in table 5.10.

| | PMMA | PU Foam |
|---|---|---|
| $E$ (MPa) | 2950 | 280 |
| $\nu$ | 0.34 | 0.302 |
| $\sigma_t$ (MPa) | 80 | 3.86 |
| $K_{IC}$ (MPa m$^{0.5}$) | 1.6 | 0.342 |
| Reference | [46] | [47] |

Table 5.10: Material properties of the investigated polymers: Polymethyl methacrylate (PMMA) and Polyurethane rigid foam (PU foam).

In analogy to the case of ceramics materials, ASED calculations data for different polymers are listed in tables 5.11 and 5.12. Only experimental loads for the case of PMMA tested by Bhattacharjee [48] were available for comparison, and are plotted together with finite elements prediction in figure 5.11.

Moreover, Stress Intensity factors, numerically obtained for different materials, are illustrated in figures 5.11 and 5.12 and compared with values reported in literature.

In the case of PMMA FPB specimens, the FE model did not provide a satisfactory failure prediction. As evident from table 5.11 and figure 5.11, the discrepancy ($\Delta\%$) is never less than 25% except for one mixed mode case. Particularly, with increasing mode II loading, the mismatch between experimental and numerical data exceeded 100%.

The discordance between simulations and experimental evidence is also proved by the SIFs analysis in figure 5.11. However, the fracture toughness value for pure mode I ($K_{IC}$) obtained by FE analysis, equal to 1.602, is in very good agreement with the value reported in table 5.10 for the tested PMMA, suggesting that maybe the fracture tests of PMMA were not carried out with sufficient precision.

Results regarding PU rigid foam are quite acceptable. SIFs analysis in figure 5.12 reveals that probably the failure prediction underestimates the real failure load sustained by the material, being the SIFs curve below the experimental points.

| $Me$ | $K_{1c}$ (MPa m$^{0.5}$) | $K_{2c}$ (MPa m$^{0.5}$) | $F_{FEM}$ (N) | $F_{an}$ (N) | $F_{exp}$ (N) | $\Delta\%$ (%) | $\sqrt{\frac{W}{W_c}}$ |
|---|---|---|---|---|---|---|---|
| 1 | 1.603 | 0 | 241 | 229 | 150 | 37.82 | 0.66 |
| 1 | 1.603 | 0 | 241 | 229 | 170 | 29.53 | 0.74 |
| 0.94 | 1.586 | 0.158 | 432 | 409 | 690 | 59.65 | 1.69 |
| 0.9 | 1.553 | 0.247 | 465 | 442 | 614 | 31.91 | 1.39 |
| 0.85 | 1.488 | 0.361 | 550 | 524 | 771 | 40.29 | 1.47 |
| 0.81 | 1.431 | 0.436 | 633 | 606 | 1130 | 78.39 | 1.87 |
| 0.73 | 1.291 | 0.571 | 818 | 788 | 850 | 3.90 | 1.08 |
| 0.65 | 1.12 | 0.69 | 993 | 963 | 1414 | 42.34 | 1.47 |
| 0.5 | 0.819 | 0.829 | 1206 | 1181 | 1502 | 24.51 | 1.27 |
| 0.37 | 0.598 | 0.895 | 1310 | 1289 | 1790 | 36.62 | 1.39 |
| 0.3 | 0.467 | 0.923 | 1355 | 1336 | 1970 | 45.39 | 1.47 |
| 0.21 | 0.325 | 0.945 | 1391 | 1374 | 2093 | 50.42 | 1.52 |
| 0.11 | 0.174 | 0.959 | 1417 | 1402 | 2600 | 83.47 | 1.85 |
| 0.01 | 0.017 | 0.965 | 1430 | 1415 | 2930 | 104.89 | 2.07 |

Table 5.11: Fracture parameters and failure load prediction for PMMA.

| $Me$ | $K_{Ic}$ (MPa $m^{0.5}$) | $K_{IIc}$ (MPa $m^{0.5}$) | $F_{FEM}$ (N) | $F_{an}$ (N) |
|---|---|---|---|---|
| 0.02 | 0.005 | 0.214 | 2469 | 2471 |
| 0.08 | 0.028 | 0.214 | 2462 | 2456 |
| 0.16 | 0.055 | 0.212 | 2441 | 2433 |
| 0.21 | 0.071 | 0.21 | 2421 | 2416 |
| 0.27 | 0.092 | 0.208 | 2389 | 2370 |
| 0.32 | 0.112 | 0.204 | 2350 | 2333 |
| 0.38 | 0.136 | 0.199 | 2293 | 2268 |
| 0.42 | 0.153 | 0.195 | 2243 | 2210 |
| 0.47 | 0.173 | 0.189 | 2176 | 2137 |
| 0.52 | 0.195 | 0.182 | 2090 | 2041 |
| 0.58 | 0.22 | 0.172 | 1974 | 1917 |
| 0.63 | 0.244 | 0.161 | 1845 | 1778 |
| 0.68 | 0.267 | 0.148 | 1696 | 1624 |
| 0.72 | 0.284 | 0.136 | 1560 | 1490 |
| 0.76 | 0.302 | 0.122 | 1397 | 1327 |
| 1 | 0.368 | 0 | 323 | 300 |

Table 5.12: Fracture parameters and failure load prediction for PU foam.

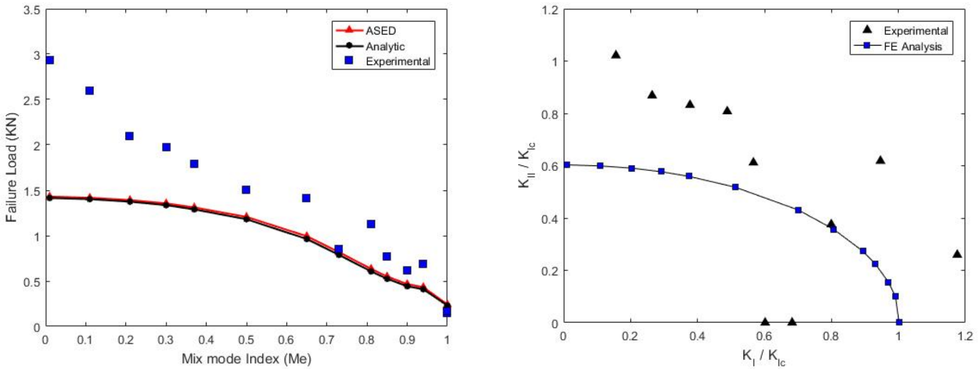

Figure 5.11: Failure prediction and SIFs analysis of PMMA.

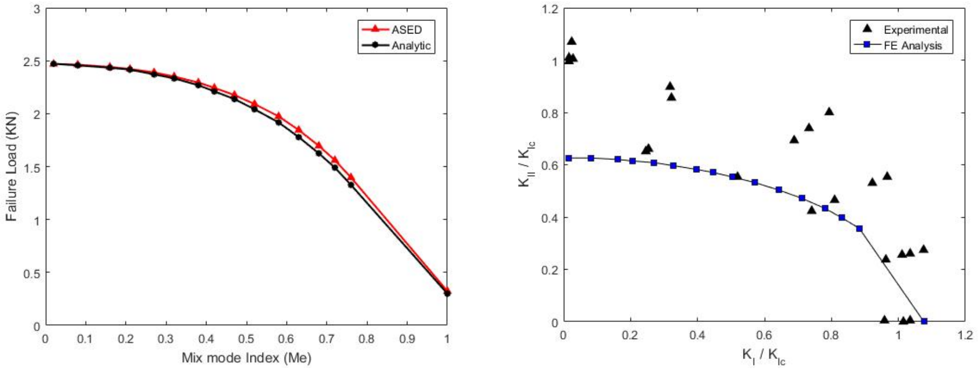

Figure 5.12: Failure prediction and SIFs analysis of PU foam.

### 5.1.3 Metallic materials

ASED calculation regarding metallic FPB specimens are presented in this section. In particular, the samples of steel listed in table 5.13 are considered.

It is important to specify that the experiments in [49] were carried out at very low temperature ($T = -196\,°\mathrm{C}$), in order to ensure that the material assumed a brittle behavior, and therefore that failure load could successfully be evaluated by means of ASED criterion.

In analogy with the case of ceramic and polymeric materials already presented, the failure load prediction is shown in figures 5.15, 5.13 and 5.14, for the different typology of steel under consideration, in function of mix mode index $Me$, and compared with experimental data.

| | En3B | 1Cr1Mo0.3V-S | 1Cr1Mo0.3V-L |
|---|---|---|---|
| $E$ (MPa) | 200000 | 200000 | 200000 |
| $\nu$ | 0.3 | 0.3 | 0.3 |
| $\sigma_t$ (MPa) | 700 | 850 | 570 |
| $K_{IC}$ (MPa $\mathrm{m}^{0.5}$) | 25 | 24 | 24 |
| Reference | [49] | [49] | [49] |

Table 5.13: Material properties of the investigated type of steel: A mild steel (En3B) and a structural steel both with small grain size (1Cr1Mo0.3V-S) and large grain size (1Cr1Mo0.3V-L).

It is worth mentioning that the failure prediction curve in figures 5.15, 5.13 and 5.14 are derived for a constant initial crack length $a = 10\,\mathrm{mm}$, hence with slightly different values than the ones reported in the respective tables, since a curve with different values of crack length would have been graphically meaningless.

In every type of tested steel, there is a quite satisfactory agreement between numerical prediction and experimental failure load. As already seen for other ceramic materials, greater discrepancies were found with increasing mode II to mode I fracture component. This fact would suggest that the mixed mode I and II might involve some phenomena of plasticity that make the fracture more complex than the standard case of pure mode I.

The failure of ASED method for prevalent shearing mode fracture is also shown in figure 5.16, where the square root ratio of averaged SED to the critical $W_c$ is plotted with varying mix mode parameter $Me$.

One would note that al lower values of $Me$ the experimental points fell above the unit value, meaning that possible large scale yielding provoked energy dissipation that hindered the crack growth.

| $Me$ | $K_{1c}$ (MPa $m^{0.5}$) | $K_{2c}$ (MPa $m^{0.5}$) | $F_{FEM}$ (KN) | $F_{an}$ (KN) | $F_{exp}$ (KN) | $a$ (mm) | $\Delta\%$ (%) | $\sqrt{\frac{W}{W_c}}$ |
|---|---|---|---|---|---|---|---|---|
| 1 | 24.12 | 0.00 | 8.0 | 8.0 | 5.8 | 10.2 | 27.76 | 0.72 |
| 1 | 24.12 | 0.00 | 8.0 | 10.1 | 6.2 | 10 | 22.78 | 0.77 |
| 0.92 | 23.86 | 2.97 | 15.2 | 18.9 | 13.8 | 10.8 | 9.09 | 0.91 |
| 0.69 | 18.57 | 9.66 | 23.9 | 30.0 | 30.6 | 9.9 | 27.95 | 1.28 |
| 0.68 | 18.27 | 9.88 | 24.4 | 30.6 | 31.9 | 9.9 | 30.86 | 1.31 |
| 0.57 | 14.72 | 11.96 | 29.1 | 36.6 | 30.2 | 10.1 | 3.75 | 1.04 |
| 0.56 | 14.47 | 12.08 | 29.4 | 36.9 | 30.4 | 10.2 | 3.42 | 1.03 |
| 0.3 | 7.34 | 14.38 | 35.1 | 44.2 | 42.7 | 10.2 | 21.52 | 1.22 |
| 0.09 | 2.25 | 15.04 | 36.9 | 46.4 | 49.5 | 12.8 | 34.01 | 1.34 |

Table 5.14: Fracture parameters and failure load prediction for structural steel 1Cr1Mo0.3V with small grain size.

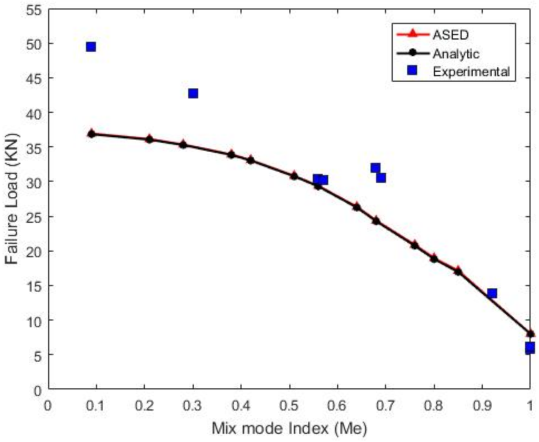

Figure 5.13: Failure prediction of structural steel 1Cr1Mo0.3V with small grain size.

| $Me$ | $K_{1c}$ (MPa m$^{0.5}$) | $K_{2c}$ (MPa m$^{0.5}$) | $F_{FEM}$ (KN) | $F_{an}$ (KN) | $F_{exp}$ (KN) | $a$ (mm) | $\Delta\%$ (%) | $\sqrt{\frac{W}{W_c}}$ |
|---|---|---|---|---|---|---|---|---|
| 1 | 24.24 | 0.00 | 8.1 | 7.9 | 5.5 | 10 | 31.84 | 0.68 |
| 1 | 24.24 | 0.00 | 8.1 | 7.9 | 6.4 | 10.2 | 20.69 | 0.79 |
| 0.93 | 24.12 | 2.78 | 15.2 | 14.8 | 10.6 | 10.2 | 30.29 | 0.70 |
| 0.92 | 23.97 | 3.21 | 15.4 | 15.0 | 13.7 | 10.4 | 11.03 | 0.89 |
| 0.71 | 19.04 | 9.37 | 23.3 | 23.0 | 18.9 | 11.8 | 18.94 | 0.81 |
| 0.56 | 14.47 | 12.08 | 29.4 | 29.1 | 31.3 | 11.6 | 6.48 | 1.06 |
| 0.38 | 9.34 | 13.88 | 33.8 | 33.6 | 41.9 | 10.2 | 23.79 | 1.24 |
| 0.38 | 9.34 | 13.88 | 33.8 | 33.6 | 40.7 | 10.2 | 20.25 | 1.20 |
| 0.25 | 6.01 | 14.57 | 35.7 | 35.5 | 41.7 | 12.4 | 16.94 | 1.17 |
| 0.17 | 4.17 | 14.82 | 36.3 | 36.1 | 59.4 | 11 | 63.48 | 1.63 |
| 0.09 | 2.25 | 14.98 | 36.8 | 36.6 | 57.7 | 11.4 | 56.77 | 1.57 |
| 0.09 | 2.25 | 14.98 | 36.8 | 36.6 | 58.9 | 11 | 60.03 | 1.60 |

Table 5.15: Fracture parameters and failure load prediction for structural steel 1Cr1Mo0.3V with large grain size.

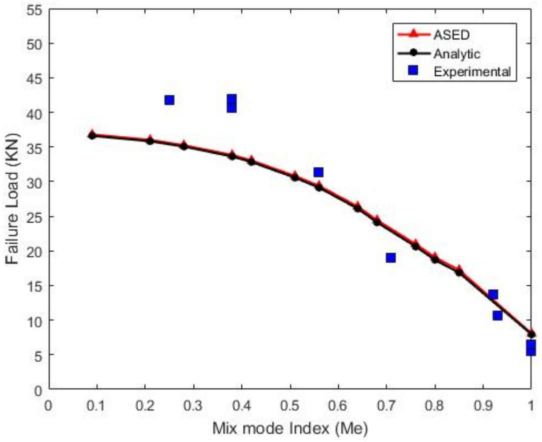

Figure 5.14: Failure prediction of structural steel 1Cr1Mo0.3V with large grain size.

| $Me$ | $K_{1c}$ (MPam$^{0.5}$) | $K_{2c}$ (MPam$^{0.5}$) | $F_{FEM}$ (KN) | $F_{an}$ (KN) | $F_{exp}$ (KN) | $a$ (mm) | $\Delta\%$ (%) | $\sqrt{\frac{W}{W_c}}$ |
|---|---|---|---|---|---|---|---|---|
| 1 | 25.16 | 0.00 | 8.3 | 8.2 | 5.7 | 10 | 31.25 | 0.69 |
| 1 | 25.16 | 0.00 | 8.3 | 8.2 | 6.1 | 10 | 26.43 | 0.74 |
| 1 | 25.15 | 0.00 | 8.2 | 8.1 | 6.6 | 10.2 | 19.16 | 0.81 |
| 0.91 | 24.72 | 3.65 | 15.5 | 15.2 | 14.3 | 10.2 | 7.51 | 0.92 |
| 0.9 | 24.55 | 4.06 | 14.8 | 14.5 | 13 | 10.3 | 12.19 | 0.88 |
| 0.69 | 19.35 | 10.08 | 26.2 | 25.9 | 29.9 | 9.3 | 14.20 | 1.14 |
| 0.7 | 19.42 | 10.01 | 23.7 | 23.5 | 28.1 | 10.2 | 18.50 | 1.18 |
| 0.57 | 15.46 | 12.37 | 27.8 | 27.7 | 31.9 | 10.6 | 14.62 | 1.15 |
| 0.54 | 14.51 | 12.81 | 30.9 | 30.7 | 38.4 | 10 | 24.38 | 1.24 |
| 0.38 | 9.74 | 14.46 | 35.3 | 35.1 | 51.4 | 10 | 45.76 | 1.46 |
| 0.38 | 9.74 | 14.46 | 34.9 | 34.8 | 50.7 | 10 | 45.23 | 1.45 |
| 0.39 | 10.18 | 14.33 | 26.5 | 26.4 | 44.2 | 12.6 | 66.70 | 1.67 |
| 0.36 | 9.37 | 14.54 | 28.6 | 28.5 | 36.5 | 11.9 | 27.56 | 1.28 |
| 0.27 | 6.84 | 15.09 | 31.5 | 31.4 | 38.8 | 11 | 23.10 | 1.23 |
| 0.23 | 5.77 | 15.26 | 33.1 | 32.9 | 50 | 11 | 51.23 | 1.51 |
| 0.21 | 5.31 | 15.33 | 37.2 | 37.0 | - | 10 | - | - |
| 0.11 | 2.75 | 15.58 | 27.3 | 27.2 | - | 13.2 | - | - |

Table 5.16: Fracture parameters and failure load prediction for En3B mild steel.

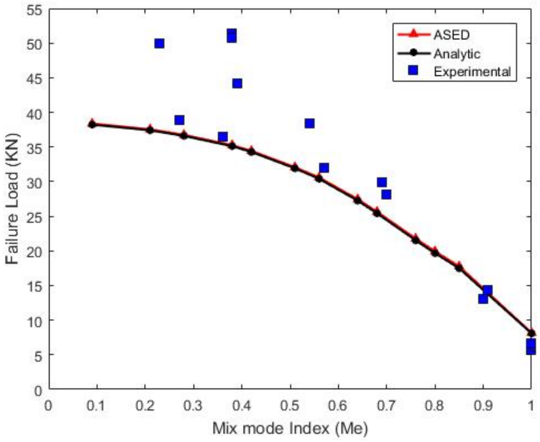

Figure 5.15: Failure prediction of En3B mild steel.

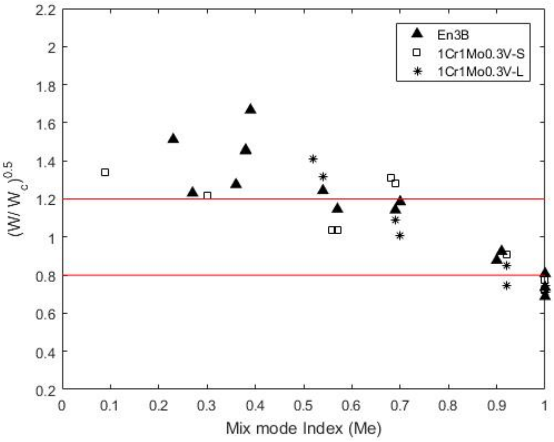

Figure 5.16: Ratio between $\overline{W}$ and $W_c$ for all the metallic materials considered in this work.

## 5.2 FVSD specimen

In table 5.17 the material properties of the PMMA constituting the investigated FVSD specimens are listed.

| | PMMA |
|---|---|
| $E$ (MPa) | 2018 |
| $\nu$ | 0.38 |
| $\sigma_t$ (MPa) | 70.5 |
| $\sigma_c$ (MPa) | 98 |
| $K_{IC}$ (MPa m$^{0.5}$) | 1.96 |
| Reference | [37] |

Table 5.17: Material properties of the the PMMA constituting the investigated FVSD specimens, where $\sigma_c$ represents the ultimate compressive strenght.

All the averaged failure loads $\overline{F}_{exp}$ obtain experimentally [35] are listed in table 5.18 for notch length $a = 10$ and 25 mm respectively, and different notch configurations. In the same table are summarized the nominal stresses $\sigma_n$ at the net transverse sectional area as well as the maximum compression stresses $\sigma_{max}$ at the notch tip, reported in literature. The peak stresses $\sigma_{max,FEM}$, obtained by finite elements analysis by considering the reported experimental load and taking advantage of linear elasticity, are also listed in the same table.

What emerged from a review of data presented in table 5.18 was that, surprisingly, the fracture load slightly increased with larger notch tip radius. For instance, in the case of $a = 25$ mm and $2\alpha = 30\,°$ there was a reduction from and averaged load of 3900 N for $\rho = 0.5$ mm, to 3550 N in the case of $\rho = 2$ mm.

When the notch length $a$ was kept constant, there was no significant variation on the load fracture with different notch opening angle $2\alpha$. Nevertheless, greater opening angle resulted in less critical failure conditions.

In the other hand, the variability of the loads with different notch length was remarkably high, due to the substantial variation of the net section area: the averaged critical load equal to 9030 N found for the case of $a = 10$ mm, $2\alpha = 30\,°$ and $\rho = 0.5$ mm drastically reduced to 3900 N extending the notch length up to $a = 25$ mm.

Despite the effect of different notch radius $\rho$ on the critical load was quite small, the variation of the elastic peak stress at the notch tip relative to the nominal compression loading was very high. For instance, values of averaged peak stresses ranged from 438 MPa up to 1080 MPa in the case of $a = 25\,\mathrm{mm}$ and $2\alpha = 90\,°$.

Therefore, the main conclusion was that the PMMA specimens, under compression loading, exhibited a low notch sensitivity, given that the peak stresses reported in table 5.18 were not able to control the failure conditions.

It is worth mentioning that in reference [50], where a similar SED analysis was carried out in the case of isostatic graphite specimens weakened by V-notches with end holes, Berto et al. found a reduction of failure load with increasing notch radius. Such phenomenon was explained by means of a reduction of the net cross section, while the effect related to the enhanced stress concentration with smaller notch radius was assumed negligible with respect to the net section area variation.

However, differently from the case studied by Berto et al., in the FVSD specimen considered in this work, the notch length $a$ was kept constant while varying the notch radius $\rho$, which resulted in a constant net section area, confirming the hypothesis that compressive failure was not related to the stress peak occurring at the notch tip.

Finally, a comparison between peak stress reported in literature and evaluated by finite element analysis listed in table 5.18 showed a good agreement between the results, suggesting a correct modelling of the experimental scenario, and encouraging the application of ASED criterion for the fracture assessment of FVSD specimens.

In the third chapter, the case of blunt notches, with particular reference to the shape and position of the control volume for SED calculation was discussed, and is used here to define its size and position in function of the notch tip radius $\rho$.

However, equation (3.13) could not be used for the case of compressive load and, at the state of the art, there was not a close analytic formula to define the control radius in the case of negative mode I fracture.

Therefore, an alternative method to define the control volume and carry out SED calculation was required.

In this work, the procedure proposed by Berto et al. [50] has been followed, according to which the control radius had to be determined empirically by considering the data related to the sets of specimens with a fixed notch opening angle and by the minimum and maximum notch tip radius. Then, by investigating different values of control radius $R_0$ and plotting the value of SED relative to different $R_0$ the intersection between the two curves was found. At the intersection, the two geometries are characterized by the same

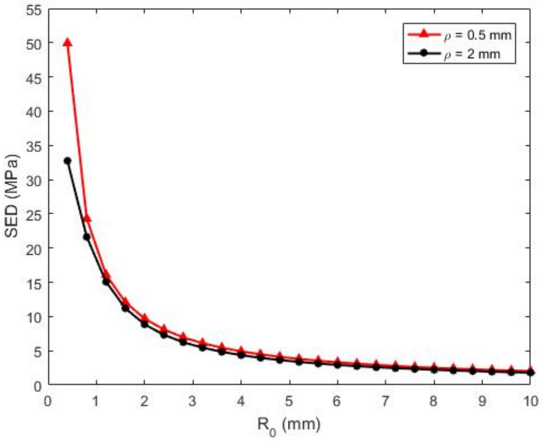

Figure 5.17: Strain energy density (SED) averaged in a volume varying with $R_0$ for $\rho = 0.5\,\mathrm{mm}$ (red line) and $\rho = 2\,\mathrm{mm}$ (black line).

value of SED, independently of the acuity and shape of the notch.

In the case of FVSD, the sets of specimens with opening angle equal to $2\alpha = 30\,°$, notch length $a$ equal to 10 mm and notch tip radius $\rho$ of 0.5 mm and 2 mm were considered. As illustrated in figure 5.17, the curves representing critical SED for the two geometries did not present a clear intersection.

However, with increasing control radius $R_0$, the discrepancy between SED relative to the curves in figure 5.17 reduced significantly, and the discrepancy decreased and became less than 8% at control radius of 1.6 mm. Therefore, values of 1.6 mm and, correspondently, 11.8 MPa were assumed as control radius $R_0$ and critical SED $W_c$ respectively to effectuate ASED calculation.

Figure 5.18 represents the elements defining the control volume and the contour plot of the elastic strain energy density (SED).

As expected from the symmetry of the problem, the maximum compressive stress and consequently the maximum strain energy density occurs at the notch tip, validating the choice of aligning the control volume with the notch bisector.

Table 5.19 summarizes all the results, including the geometrical parameters $2\alpha$, $\rho$ and $a$, the prediction of failure load $F_{FEM}$, SED obtained from finite elements analysis by applying a unit load, the correspondent critical value ($\overline{W}$ ) obtained multiplying SED by the reported averaged experimental load $\overline{F}_{exp}$, and the square root of the ratio between $\overline{W}$ and $W_c$.

In order to provide a better comparison of results, failure predictions are also illustrated, for each set of specimens, in figure 5.20, where values of failure load from experiments and numerical analysis were compared in

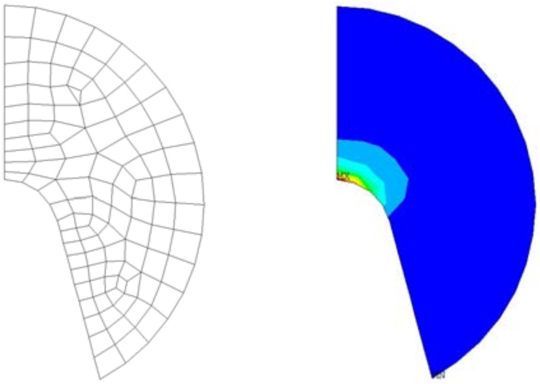

Figure 5.18: Elements defining the control volume and strain energy contour for the FVSD specimen with $a = 10\,\text{mm}$, $2\alpha = 30\,^\circ$ and $\rho = 0.5\,\text{mm}$.

function of the notch tip radius.

What emerges from analysis of figure 5.20 and table 5.19 is that the implemented ASED method partially fulfilled the assessment of failure for the tested FVSD specimens.

According to FE elements, and from an engineering point of view, the notch sensitivity for the explored samples was null. An extremely low variation of failure load was found in function of notch tip radius $\rho$ and the dependency of the opening angle $2\alpha$ was quite small, both for $a = 10\,\text{mm}$ and $a = 25\,\text{mm}$.

In the case of $a = 10\,\text{mm}$, and $\rho = 1\,\text{mm}$ the failure predicted by FE model overestimated the real ultimate load, although the entity of such discrepancy was relatively small. In general, the implemented numerical model was not able to assess the initial decrease of failure from $\rho = 0.5\,\text{mm}$ to $\rho = 1\,\text{mm}$ and its successive increase with larger $\rho$, but showed instead a slightly monotonic decrease of failure with the notch tip radius.

A possible explanation of this phenomenon could be that the fracture resistance of the specimen, tested under compressive loading, had to be related to the entire volume of the sample rather than to the stress concentration at the notch tip.

As a matter of fact, the increment of $\rho$ resulted in a moderate decrease of the volume of the specimen, which might account for the slightly reduction of the ultimate load. It is worth to mention that despite the very low notch sensitivity presented by FVSD specimens, fracture phenomenon was not controlled by the nominal stress at the net transverse section as one would note by observing the value of the experimental nominal stresses ($\sigma_n$) listed in table 5.18.

The variation of $\sigma_n$ with opening angle $2\alpha$ and notch radius $\rho$ was obviously quite small (which results from the already discussed poor variation of failure load and constant transverse section) and ranged from 26.5 MPa to 37.6 MPa, in the case of $a = 10$ mm, and from 18.3 MPa to 26.4 MPa for $a = 25$ mm. However, such values of stresses are not comparable with the ultimate compressive strength reported for the tested PMMA as equal as 98 MPa.

In light of these observations, ASED method implemented in this work, could be seen as link between a pure local approach where the relevant parameter was the peak stress occurring at the notch tip, and a merely nominal approach, based on the nominal stress at the net transverse section.

Figure 5.19 shows different values of the square root of $\overline{W}/W_c$ showing that the majority of the experimental values obtained for PMMA specimen fell inside a scatterband ranging from 0.8 to 1.2.

This validates the hypothesis that an energy-based approach such as ASED method was able to successfully evaluated the fracture phenomenon occurring in brittle or quasi-brittle materials, independently from the notch sensitivity.

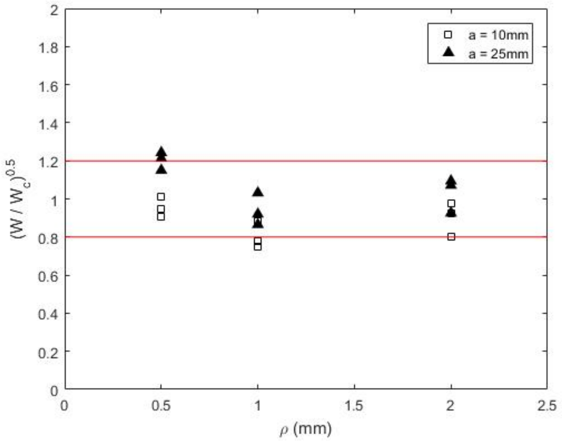

Figure 5.19: SED scatterband relative to FVSD specimens with different notch shape in function of $\rho$.

| $a$ (mm) | $2\alpha$ (deg) | $\rho$ (mm) | $F_{exp}$ (N) | $\sigma_{max}$ (MPa) | $\sigma_{max,FEM}$ (MPa) | $\sigma_n$ (MPa) |
|---|---|---|---|---|---|---|
| 10 | 30 | 0.5 | 9030 | -1002 | -919 | 37.6 |
| | | 1 | 6877 | -548 | -535 | 28.7 |
| | | 2 | 8400 | -492 | -489 | 35.0 |
| | 60 | 0.5 | 7703 | -849 | -889 | 32.1 |
| | | 1 | 6357 | -507 | -490 | 26.5 |
| | | 2 | 7720 | -450 | -411 | 32.2 |
| | 90 | 0.5 | 7787 | -823 | -812 | 32.4 |
| | | 1 | 7287 | -567 | -579 | 30.4 |
| | | 2 | 6603 | -380 | -365 | 27.5 |
| 25 | 30 | 0.5 | 3893 | -1169 | -1130 | 26.0 |
| | | 1 | 3080 | -634 | -629 | 20.5 |
| | | 2 | 3547 | -532 | -556 | 23.6 |
| | 60 | 0.5 | 3947 | -961 | -1043 | 26.3 |
| | | 1 | 3347 | -673 | -664 | 22.3 |
| | | 2 | 3423 | -516 | -528 | 22.8 |
| | 90 | 0.5 | 3963 | -1083 | -1084 | 26.4 |
| | | 1 | 2750 | -546 | -488 | 18.3 |
| | | 2 | 2960 | -438 | -405 | 19.7 |

Table 5.18: Experimental failure load and peak stresses values for FVSD specimen according to [35], together with calculated nominal compressive stress at the net transverse section and stress peak from numerical analysis.

| $a$<br>(mm) | $2\alpha$<br>(deg) | $\rho$<br>(mm) | SED<br>(MPa) | $F_{FEM}$<br>(N) | $\overline{F}_{exp}$<br>(N) | $\overline{W}$<br>(MPa) | $\sqrt{\frac{\overline{W}}{W_c}}$ |
|---|---|---|---|---|---|---|---|
| 10 | 30 | 0.5 | 0.1482 | 8923 | 9030 | 12.08 | 1.01 |
| | | 1 | 0.1507 | 8848 | 6877 | 7.13 | 0.78 |
| | | 2 | 0.1588 | 8622 | 8400 | 11.20 | 0.97 |
| | 60 | 0.5 | 0.1626 | 8520 | 7703 | 9.65 | 0.90 |
| | | 1 | 0.1640 | 8481 | 6357 | 6.63 | 0.75 |
| | | 2 | 0.1684 | 8372 | 7720 | 10.03 | 0.92 |
| | 90 | 0.5 | 0.1736 | 8245 | 7786 | 10.52 | 0.94 |
| | | 1 | 0.1736 | 8244 | 7287 | 9.22 | 0.88 |
| | | 2 | 0.1741 | 8232 | 6603 | 7.59 | 0.80 |
| 25 | 30 | 0.5 | 1.0306 | 3384 | 3893 | 15.62 | 1.15 |
| | | 1 | 1.0542 | 3346 | 3080 | 10.00 | 0.92 |
| | | 2 | 1.1226 | 3242 | 3547 | 14.12 | 1.09 |
| | 60 | 0.5 | 1.1166 | 3251 | 3946 | 17.39 | 1.21 |
| | | 1 | 1.1214 | 3244 | 3347 | 12.56 | 1.03 |
| | | 2 | 1.1560 | 3195 | 3423 | 13.54 | 1.07 |
| | 90 | 0.5 | 1.1610 | 3188 | 3963 | 18.23 | 1.24 |
| | | 1 | 1.1684 | 3178 | 2750 | 8.84 | 0.87 |
| | | 2 | 1.1548 | 3197 | 2960 | 10.12 | 0.93 |

Table 5.19: ASED results for different geometries of FVSD.

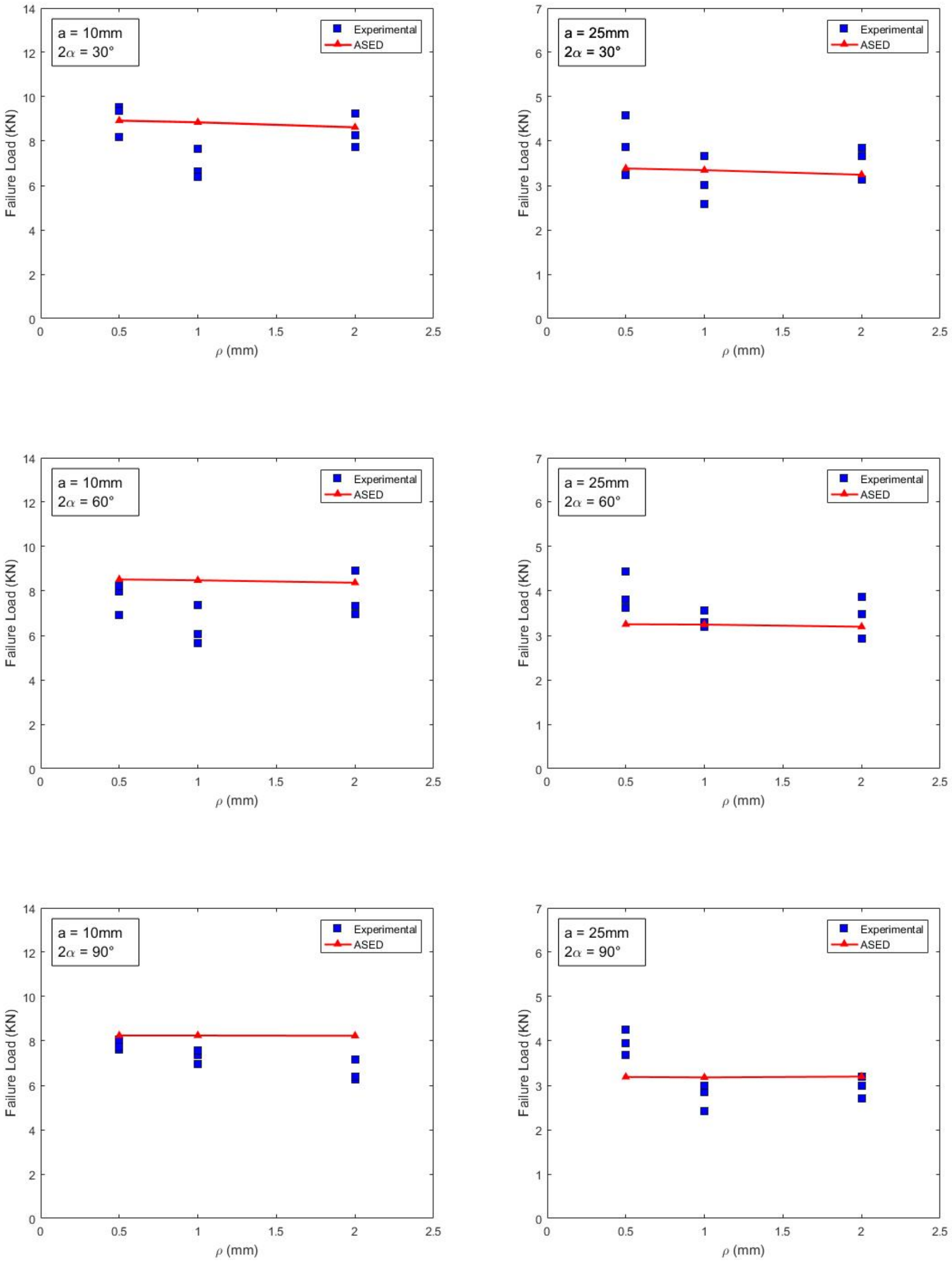

Figure 5.20: Failure prediction of FVSD specimen for different notch geometries, in function of notch tip radius $\rho$.

## 5.3 RVBD specimen

Differently from the case of FVSD specimen, concerning the investigation of pure compressive mode I, outcomes from RVBD tests are useful to understand the mechanism of mixed mode I and II loading with negative mode I component.

In table 5.20 the material properties of the PMMA constituting the RVBD specimen under study are listed.

| | PMMA |
|---|---|
| $E$ (MPa) | 1816 |
| $\nu$ | 0.38 |
| $\sigma_t$ (MPa) | 68.5 |
| $\sigma_c$ (MPa) | 100.5 |
| $K_{IC}$ (MPa m$^{0.5}$) | 1.71 |
| Reference | [39] |

Table 5.20: Material properties of the PMMA constituting the investigated RVBD specimens.

Figure 5.21 shows the elements defining the control volume with crescent shape for the case of $2\alpha = 30\,^\circ$ and $\rho = 1\,\text{mm}$ together with the contour plot of strain energy density (SED).

As discussed in the previous chapter, the modelling of the control volume where the maximum first principal stress occurred (and therefore the maximum SED), was consistent with the experimental evidence reporting a crack initiation from the right half border of the round V-notch, where a tensile field stress was revealed by FE analysis.

It is interesting to note that in the case of $\beta = 30\,^\circ$, described in figure 5.21, the maximum principal stress arose near the extreme right border of the V-notch, which fact resulted in a control volume that embraced part of the straight notch flank. This effect was even enhanced with increasing value of loading angle $\beta$.

All the averaged failure loads $\overline{F}_{exp}$ obtained experimentally [39], together with the prediction from finite element analysis ($F_{FEM}$), are listed in tables 5.21 and 5.22 for $2\alpha = 30\,^\circ$ and $2\alpha = 60\,^\circ$ respectively. Such results are also graphically illustrated in figures 5.23 and 5.24 for different cases of notch

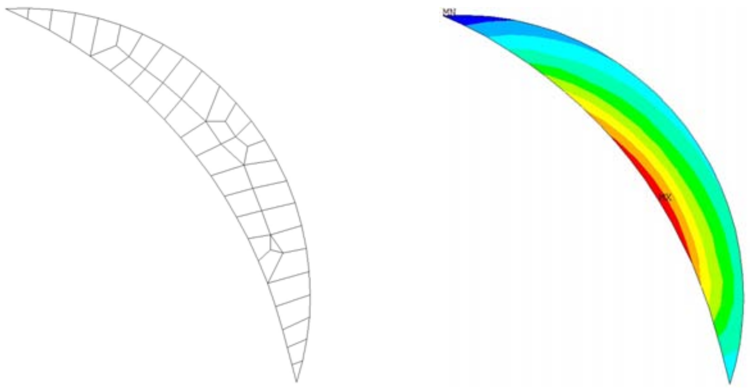

Figure 5.21: Elements defining the control volume and strain energy contour for the RVBD specimen with $2\alpha = 30\,°$, $\rho = 1\,\mathrm{mm}$ and $\beta = 30\,°$.

angles $2\alpha$ and loading angles $\beta$, where fracture load is plotted in function of the notch tip radius $\rho$.

For every set of data, there was an excellent agreement between the finite element analysis and the experimental results, meaning that the ASED method successfully described the fracture phenomenon of RVBD specimens.

In addition, different square root values of the ratio $\overline{W}/W_c$ are plotted with varying notch radius $\rho$ in figure 5.22, showing that the entire set of experimental data of tested PMMA are inside the range from 0.8 to 1.2.

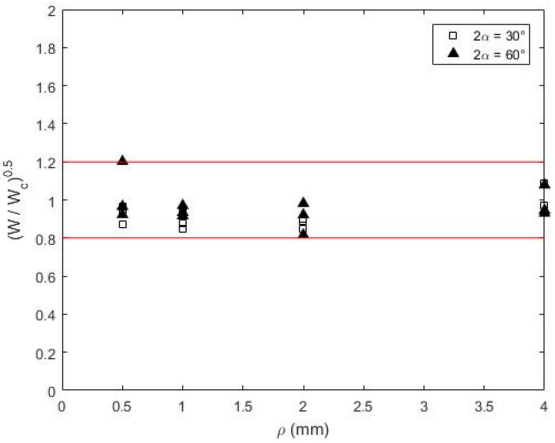

Figure 5.22: SED scatterband relative to RVBD specimens with notch opening angle $2\alpha = 30$ and $60\,°$, in function of $\rho$.

| $\rho$ (mm) | $\beta$ (°) | $F_{FEM}$ (KN) | $\overline{F}_{exp}$ (KN) | $\Delta\%$ | $\sqrt{\dfrac{\overline{W}}{W_c}}$ |
|---|---|---|---|---|---|
| 0.5 | 30 | 3.863 | 3.717 | 3.77 | 0.96 |
| | 40 | 4.944 | 4.692 | 5.09 | 0.95 |
| | 50 | 7.990 | 6.972 | 12.75 | 0.87 |
| 1 | 30 | 4.012 | 3.517 | 12.34 | 0.88 |
| | 40 | 4.995 | 4.248 | 14.95 | 0.85 |
| | 50 | 7.476 | 7.004 | 6.31 | 0.94 |
| 2 | 30 | 4.299 | 3.869 | 10.01 | 0.90 |
| | 40 | 5.102 | 4.52 | 11.41 | 0.89 |
| | 50 | 7.007 | 5.96 | 14.94 | 0.85 |
| 4 | 30 | 4.673 | 4.526 | 3.14 | 0.97 |
| | 40 | 5.068 | 5.496 | 8.44 | 1.08 |
| | 50 | 6.218 | 6.018 | 3.22 | 0.97 |

Table 5.21: Results of ASED calculation for RVBD specimen with $2\alpha = 30\,^{\circ}$.

| $\rho$ (mm) | $\beta$ (°) | $F_{FEM}$ (KN) | $\overline{F}_{exp}$ (KN) | $\Delta\%$ | $\sqrt{\frac{\overline{W}}{W_c}}$ |
|---|---|---|---|---|---|
| 0.5 | 30 | 4.629 | 4.271 | 7.72 | 0.92 |
| | 40 | 8.661 | 8.368 | 3.38 | 0.97 |
| | 45 | 9.234 | 11.097 | 20.18 | 1.20 |
| 1 | 30 | 4.578 | 4.194 | 8.38 | 0.92 |
| | 40 | 7.815 | 7.296 | 6.64 | 0.93 |
| | 45 | 9.142 | 8.871 | 2.97 | 0.97 |
| 2 | 30 | 4.596 | 4.234 | 7.87 | 0.92 |
| | 40 | 6.759 | 6.634 | 1.85 | 0.98 |
| | 45 | 8.882 | 7.252 | 18.35 | 0.82 |
| 4 | 30 | 4.600 | 4.961 | 7.84 | 1.08 |
| | 40 | 5.958 | 5.631 | 5.49 | 0.95 |
| | 45 | 7.279 | 6.774 | 6.94 | 0.93 |

Table 5.22: Results of ASED calculation for RVBD specimen with $2\alpha = 60\,°$.

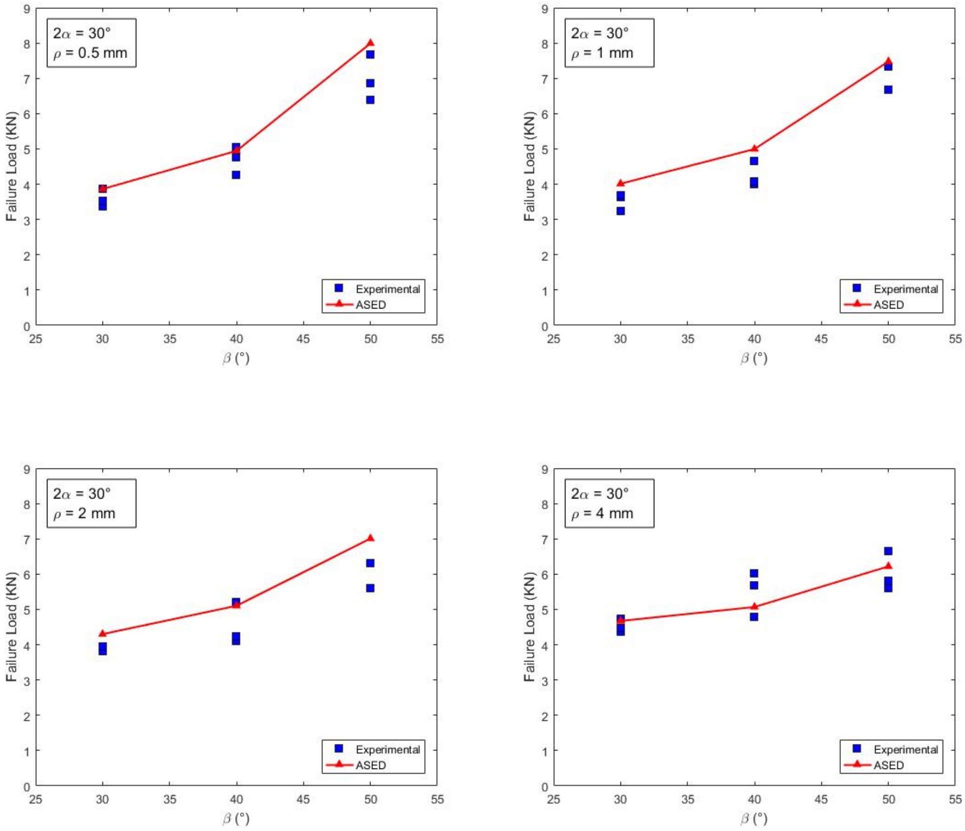

Figure 5.23: Failure prediction of RVBD specimen with $2\alpha = 30\,^{\circ}$ for different notch tip radius $\rho$, in function of loading angle $\beta$.

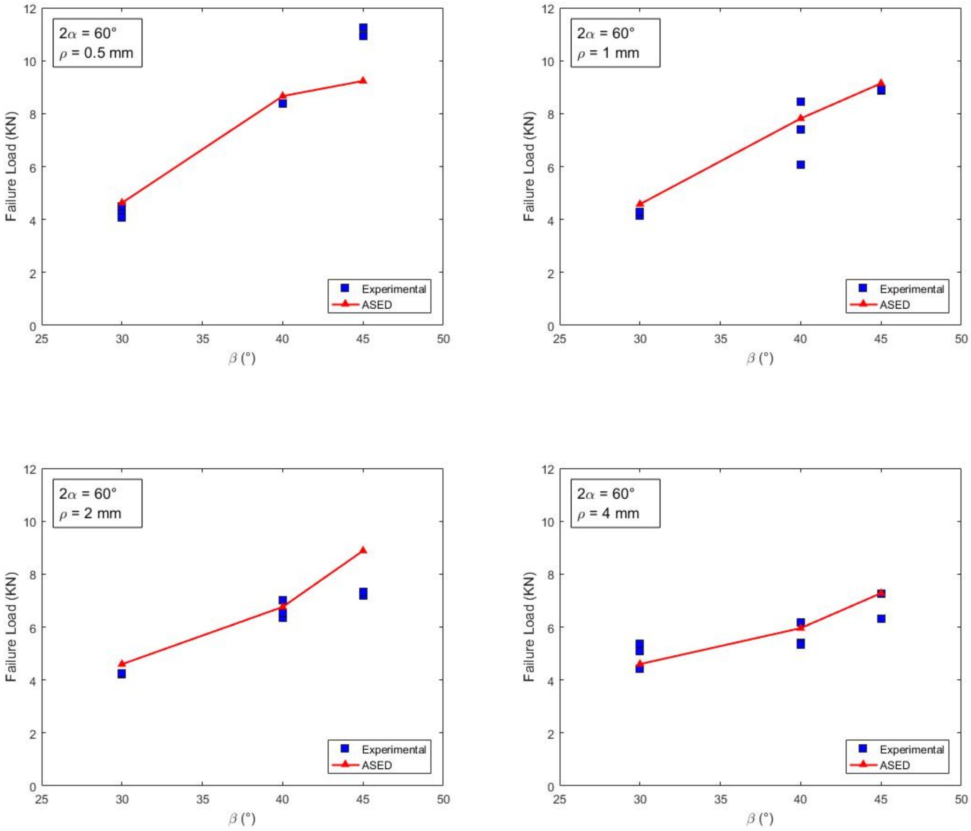

Figure 5.24: Failure prediction of RVBD specimen with $2\alpha = 60\,^\circ$ for different notch tip radius $\rho$, in function of loading angle $\beta$.

## 5.4 Mix Mode I & III

We present here the results concerning the case of mixed mode loading I and III, which modeling procedure had been explained in detailed in the previous chapter.

The experimental reference test [40] is a cracked PMMA specimen depicted in figures 4.8 and 4.10 with the material properties shown in table 5.23.

| | PMMA |
|---|---|
| $E$ (MPa) | 2959 |
| $\nu$ | 0.34 |
| $\sigma_t$ (MPa) | 55 |
| $\sigma_c$ (MPa) | 33.6 |
| $K_{IC}$ (MPa $\mathrm{m}^{0.5}$) | 1.72 |
| $K_{IIIC}$ (MPa $\mathrm{m}^{0.5}$) | 1.884 |
| Reference | [40] |

Table 5.23: Material properties of the PMMA constituting specimen for mixed mode I and III investigation.

Figure 5.25 shows the contour plot of the equivalent stress according to Von Mises criterion. Since the numerical model considered the material to assume a perfect linear elastic behavior, the contour plot of Von Mises stress qualitatively described the nominal plastic zone shapes around the crack tip.

Such shapes were comparable with the ones reported for a similar FE analysis in [40], suggesting a correct implementation of the numerical model employed in this work.

Moreover, figure 5.25 reveals that the size of crack tip plastic zone became larger with increasing contribution of mode III fracture relative to mode I.

This fact supported the idea that an alternative ASED calculation based on an 'apparent' value of SED, in order to take into account the large scale yielding occurring at the crack tip with increasing mode III fracture, might represent a correct approach for failure assessment.

As explained in the fourth chapter, some extensions of the ASED method employed in the case of two-dimensional models had to be done dealing with out of plane loading.

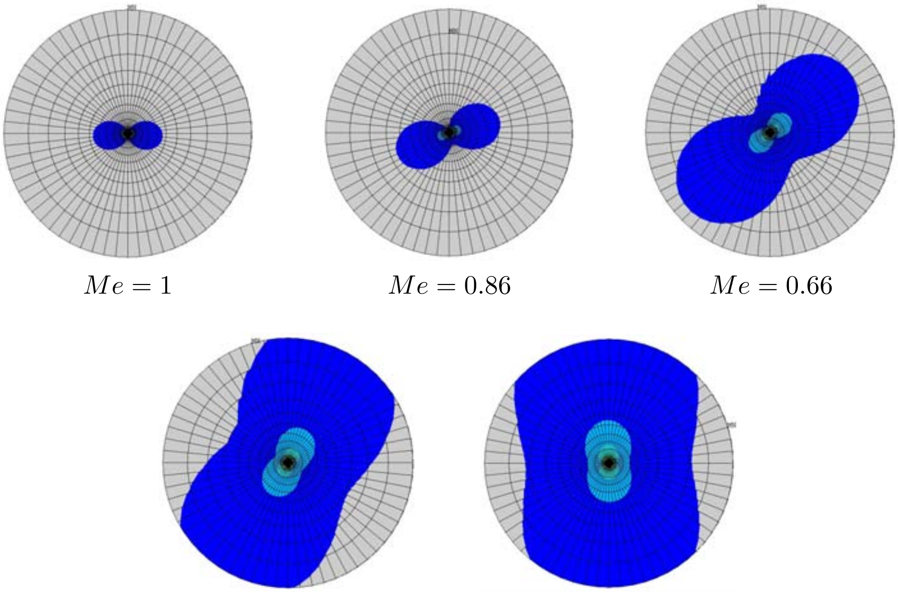

$Me = 1$ $Me = 0.86$ $Me = 0.66$

$Me = 0.32$ $Me = 0$

Figure 5.25: Contour plot of equivalent Von Mises Stress in the elements surrounding the crack tip, showing different shape and size of plastic zone with varying loading condition from pure mode I ($Me = 1$) to pure mode III ($Me = 0$).

In particular, according to the procedure reported in [51], two values of critical radius, $R_{0,I}$ and $R_{0,III}$, were calculated for mode I and mode III respectively, by means of equation (3.13) and (4.4). $R_{0,I}$ was found to be equal to 0.238 mm while $R_{0,III}$ was calculated to be 0.971 mm.

A value of 0.513 MPa was found for the critical strain energy density $W_c$ through equation (3.10).

Table 5.24 shows all the ASED parameters derived by the analysis, including the X ($x_{dis}$) and Z ($z_{dis}$) displacement recorded as preliminary results (see the numerical procedure described in the previous chapter for more details), the 'apparent' SED related to mode I ($SED_1$) and III ($SED_3$), and the final failure prediction in terms of critical load ($F_{FEM}$).

Experimental failure load and mix mode index $Me$ are available in literature and here resumed in table 5.24. Differently from the case of mixed mode I and II, now $Me = 1$ accounts for pure mode I conditions while $Me = 0$ stands for pure mode III.

For a better comparison of results, prediction and experimental load are graphically illustrated in figure 5.26 in function of $Me$.

| $Me$ | $SED_1$ (Pa) | $SED_3$ (Pa) | $X_{disp}$ (mm) | $Z_{disp}$ (mm) | $F_{FEM}$ (N) | $\overline{F}_{exp}$ (N) | $\Delta\%$ (%) |
|---|---|---|---|---|---|---|---|
| 1.00 | 1.851 | 0.000 | 5.87E-04 | 0 | 526 | 486 | 7.58 |
| 0.86 | 2.435 | 0.037 | 6.61E-04 | -5.55E-04 | 455 | 471 | 3.36 |
| 0.66 | 2.294 | 0.257 | 6.85E-04 | -1.47E-03 | 448 | 582 | 29.84 |
| 0.32 | 0.752 | 0.592 | 4.73E-04 | -2.23E-03 | 618 | 670 | 8.51 |
| 0.00 | 0.000 | 0.779 | 0 | -2.56E-03 | 811 | 737 | 9.18 |

Table 5.24: ASED parameter for the specimen tested under mixed mode I and III.

The agreement between the FE prediction and the experimental results was quite satisfactory. What emerged from analysis of table 5.24 and figure 5.26, was that the discrepancy of data is under 10% of error, except in the case of $\alpha = 65\,^\circ$ ($Me = 0.66$).

However, important considerations should be done for the reported results.

For instance, while the FE model defined that the most critical loading configuration was the one correspondent to $\alpha = 65\,^\circ$, Ayatollahi and Saboori [40] found the smallest value of failure load for $\alpha = 40\,^\circ$. Hence, both experimental and numerical investigation, revealed that pure mode I condition for the tested PMMA was less critical than a combination of opening and tearing fracture mode, meaning that the phenomenon of mixed loading I and III might deserve more attention in future investigations.

However, while the experimental nature of such initial decrease of failure load with increasing out of plane fracture might be unclear, the explanation of FE results was relatively straightforward: observing table 5.24, one would note that from $Me = 1$ to $Me = 0.66$ the displacement in $x$ direction ($X_{disp}$), arising from the unit load applied to the model, increases.

This fact was quite surprising, since apparently the application of a force decomposed in direction $x$ and $z$ (as in the case of mixed mode loading) would result into a smaller displacement in $X_{disp}$, with respect to the case of pure mode I (where the entire load is applied along the $x$ direction). Obviously, a greater component of $x$ displacement would result into a higher value of strain energy density $SED_1$, and consequently in a lower value of predicted failure.

Unfortunately, in literature only the curve load vs. displacement for the

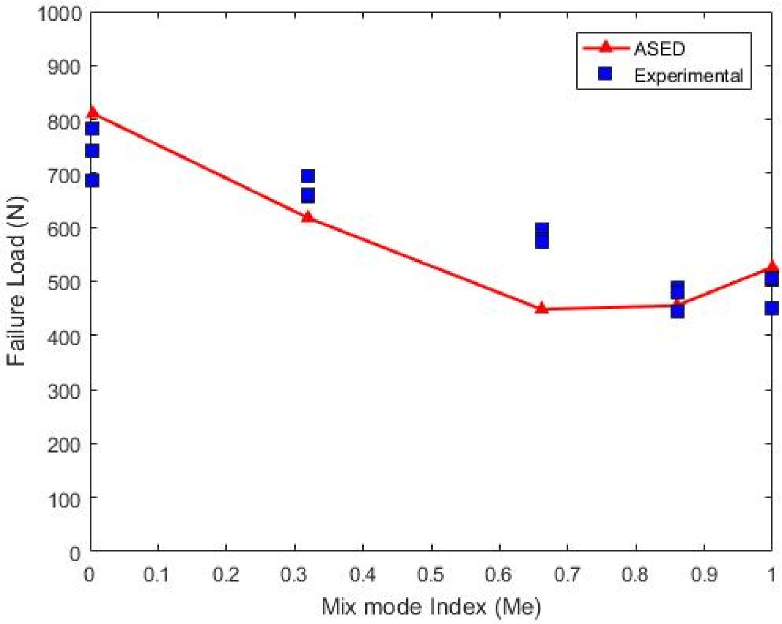

Figure 5.26: Failure prediction for the PMMA specimen tested under mixed mode I and III loading.

case of pure mode III was available, where the $z$ displacement at fracture was measured to be 4.42 mm [40]. Therefore, a comparison between experimental and numerical displacement for the mixed mode loading cases was missing.

However, taking into consideration $Z_{disp}$ obtained by numerical analysis for the case of pure mode III ($Me = 0$) , and multiplying by either the experimental of prediction failure load, the failure displacement resulted to be about 2 mm, far from 4.42 mm reported in literature. This means that although the implemented numerical model was able to provide a good assessment of the failure of PMMA under mixed mode I and III, further inspections are required to check the veracity of the analysis.

It is also worth to mention that, in principle, a larger plastic zone detected for mode III (see figure 5.25) would results into a larger energy dissipation, and therefore into a greater fracture toughness for mode III with respect to mode I. However, the fact that the most critical scenario turned out to be a mixture of mode I and III loading conditions ($Me = 0.86$ from experimental tests and $Me = 0.66$ from FE analysis), seemed to reveal that different modes of fracture cannot be considered independently one from each other.

This consideration might represent the subject of future investigations.

# Conclusions and outlook

In summary, ASED method has been implemented in this work to describe the failure phenomenon of different materials tested with several experimental apparatus.

The case of in plane mixed mode loading I and II has been discussed by studying four point bending tests of isotropic materials ranging from ceramics to polymers and metals. It emerged that a local approach based on the strain energy density evaluated in a defined control volume centered at the notch tip, was sufficiently able to assess the failure of different class of brittle materials.

Other experimental tests were successively simulated by means of numerical analysis including the case of flattened V-notch semi disk specimen, where the ASED method was employed for the first time to evaluate cases of pure compressive mode I loading. The large dimensions of the control volume found for the tested polymer suggested that ASED method might constitute a link from point-wise failure assessment methods and approaches based on nominal stresses.

In addition, the case of mixed mode I and II with negative mode I components was investigated by means of Round tip V-notch PMMA specimens. ASED criterion was able to successfully predict the fracture load, showing an excellent agreement between numerical and experimental results.

Finally, the more complex case of out of plane loading has been studied in this thesis by a numerical implementation of ASED method to assess three-dimensional problems, studied through a novelty experimental fixture.

The method was extended to the case of mixed mode I and III by introducing the concept of 'apparent' strain energy density, and numerically implemented by means of an approach which considered the decomposition of mode I and III fracture by means of displacements.

However, the study of mixed mode fracture carried out in this work gave risen to further field of research that would deserve deeper investigations.

Concerning the plane problem, the phenomenon of plasticity with increasing mode II to mode I fracture represents a limit for the application of ASED method. A possible extension of the method to evaluate case of large scale yielding would be the definition of a control volume which dimensions depend not only on the material, but also on the loading mode.

Alternatively, an idea would be to recognize as failure parameters different components of strain energy density, dependent on the particular fracture phenomenon, in order to better define a critical value of strain energy density that precisely accounts for the external boundary conditions.

On the other hand, there is a substantial lack of knowledge regarding the three-dimensional problem of mixed mode I and III fracture. More powerful analytic formulation for the stress analysis and larger experimental databases would be required to allow a better understanding of the phenomenon.

Finally, the finite elements model created in this work would need some improvements to better predict the experimental evidence both in term of failure load and displacements.

# Bibliography

[1] Duga, J.J., Fisher, W.H., Buxbaum, R. W. The Economic Effects of Fracture in the United States. (1983).

[2] Anderson, T. L. Fracture Mechanics: Foundamentals and Application. (2005).

[3] Shank, M. E. A Critical Survey of Brittle Failure in Carbon Plate Steel Structures Other Than Ships. Met. Prog. 66, 83-88 (1954).

[4] Uccelli, A. Leonardo da Vinci. Reynaland Company Inc. (1956).

[5] Griffith, A. A. The phenomena of rupture and flow in solids. Phil. Trans. Ser. A 221, 163-198 (1920).

[6] Inglis, C. E. Stresses in a plate Due to the presence of cracks and sharp corners. Trans. Inst. Nav. Archit. 55, 219-241 (1913).

[7] Kirsch, E.G., Die Theorie der Elastizität und die Bedürfnisse der Festigkeitslehre. Zeitschrift des Vereines deutscher Ingenieure, 42, 797-807 (1898).

[8] Irwin, G. R. Fracture dynamics. Fract. Met. American S, 147-166 (1948).

[9] Orowan, E. Fracture and Strength of Solids. Reports Prog. Phys. 12, 185-232 (1948).

[10] Irwin, G. R. Onset of fast crack propagation in high strength steel and aluminum alloys. Naval Research Lab Washington DC (1956).

[11] Williams, M. L. Stress singularities resulting from various boundary conditions in angular comers of plates in extension. J. Appl. Mech. 526-528 (1952).

[12] Williams, M. L. On the stress distribution at the base of a stationary crack. J. Appl. Mech. 24, 109-114 (1957).

[13] Rice, J. R. A path independent integral and the approximate analysis of strain concentration by notches and cracks. ASME J. Appl. Mech. 35, 379-386 (1968).

[14] Livieri, P. A new path independent integral applied to notched components under mode I loadings. Int. J. Fracture 123, 107-125 (2003).

[15] Haddad, M. H. E. L., Smith, K. N., Topper, T. H. Fatigue Crack Propagation of Short Cracks. J. Eng. Mater. Technol. 101, 42-46 (1979).

[16] Taylor, D., Cornetti, P., Pugno, N. The fracture mechanics of finite crack extension. Eng. Fract. Mech. 72, 1021-1038 (2005).

[17] Lazzarin, P. Zambardi, R. A finite-volume-energy based approach to predict the static and fatigue behavior of components with sharp V-shaped notches. Int. J. Fracture 112, 275-298 (2001).

[18] Lazzarin, P. Berto, F. Some expressions for the strain energy in a finite volume surrounding the root of blunt V-notches. Int. J. Fracture 135, 161-185 (2005).

[19] Neuber, H. Theory of Notch Stresses: Principles for Exact Calculation of Strength with Reference to Structural Form and Material. (1958).

[20] Westergaard, H.M., Bearing Pressures and Cracks. Journal of Applied Mechanics. 6, 49-53 (1939)

[21] Gross, B., Mendelson, A. Plane Elastostatic Analysis of V-Notched Plates. Int. J. Fract. Mech. 8, 267-276 (1972).

[22] Dunn, M.L., Suwito, W. Stress Intensities at Notch Singularities. Eng. Fract. Mech. 57, 417-430 (1997).

[23] Muskhelishvili, N. I. Singular Integral Equations. Ltd. (1953).

[24] Lazzarin, P., Tovo, R. A notch intensity factor approach to the stress analysis of welds. Fatigue Fract. Eng. Mater. Struct. 21, 1089-1103 (1998).

[25] H.England, A. Complex variable methods in elasticity. (1971).

[26] Lazzarin, P., Zappalorto, M. A three-dimensional stress field solution for pointed and sharply radiused V-notches in plates of finite thickness. Fatig. Fract. Eng. Mater. Struct. 35, 1105-1119 (2012).

[27] Beltrami, E. Rend. R. Ist. Lombardo di Scienze, Lett. Arti 18 (1885) (in Italian).

[28] Glinka, G. Energy density approach to calculation of inelastic strain-stress near notches and cracks. Eng. Fract. Mech. 22, 485-508 (1985).

[29] Molski, K., Glinka, G. A method of elastic-plastic stress and strain calculation at a notch root. Mater. Sci. Eng. 50, 93-100 (1981).

[30] Sih, G. C. Mechanics of fracture initiation and propagation: surface and volume energy density applied as failure criterion. Springer Science & Business Media (2012).

[31] G.C. Sih, in: G.C. Sih (Ed.), A Special Theory of Crack Propagation: Methods of Analysis and Solutions of Crack Problems, Mechanics of Fracture, Noordhoff, International Publishing, Leyden, pp. 21-45 (1973).

[32] Yosibash, Z., Bussiba, A., Gilad, I. Failure criteria for brittle elastic materials. Int. J. Fract. 125, 307-333 (2004)

[33] Berto, F., Lazzarin, P., Gomez, F.J., Elices, M. Fracture assessment of U-notches under mixed mode loading: two procedures based on the 'equivalent local mode I' concept. Int. J. Fract. 148, 415-433 (2007).

[34] Ayatollahi, M.R., Berto, F., Lazzarin, P. Mixed mode brittle fracture of sharp and blunt V-notches in polycrystalline graphite. Carbon, 49, 2465-2474 (2011).

[35] Torabi, A. R., Firoozabadi, M., Ayatollahi, M. R. Brittle fracture analysis of blunt V-notches under compression. Int. J. Solids Struct. 67-68, 219-230 (2015).

[36] Ayatollahi, M. R., Torabi, A. R. Tensile fracture in notched polycrystalline graphite specimens. Carbon, 48, 2255-2265 (2010).

[37] Ayatollahi, M. R., Torabi, A. R. Investigation of mixed mode brittle fracture in rounded-tip V-notched components. Eng. Fract. Mech. 77, 3087-3104 (2010).

[38] Ayatollahi, M. R., Torabi, A. R. Experimental verification of RV-MTS model for fracture in soda-lime glass weakened by a V-notch. J. Mech. Sci. Tech. 25, 2529-2534 (2011).

[39] Torabi, A. R., Bahrami. B., Ayatollahi, M. R. Mixed mode I/II brittle fracture in V-notched Brazilian disk specimens under negative mode I conditions. Phys. Mesomech. 19(3), 332-348 (2016).

[40] Ayatollahi, M. R., Saboori, B. A new fixture for fracture tests under mixed mode I/III loading. Eur. J. Mech. - A/Solids, 51, 67-76 (2015).

[41] Susmel, L., Taylor, D. The theory of critical distances to predict static strength of notched brittle components subjected to mixed-mode loading. Eng. Fract. Mech. 75, 534-550 (2008).

[42] Berto, F., Elices, M., Lazzarin, P., Zappalorto, M. Fracture behaviour of notched round bars made of PMMA subjected to torsion at room temperature. Eng. Fract. Mech. 90, 143-160 (2012).

[43] Wang, C., Zhu, Z. M., Liu, H. J. On the I-II mixed mode fracture of granite using four-point bend specimen. Fatigue Fract Engng Mater Struct, 00, 1-11 (2016).

[44] Xeidakis, G. S., Samaras, I. S., Zacharopoulos, D. A., Papakaliatakis, G. E. Trajectories of Unstably Growing Cracks in Mixed Mode I-II Loading of Marble Beams. Rock Mech. Rock Engng. 30(1), 19-33 (1997)

[45] Li, M., Sakai, M., Mixed-Mode Fracture of Ceramics in Asymmetric Four-Point Bending: Effect of Crack-Face Grain Interlocking/Bridging. J. Am. Ceram. Soc. 79(10), 2718-2726 (1996).

[46] Maccagno, T.M., Knott, J. F. The Fracture Behaviour of PMMA in mixed modes I and II. Eng. Fract. Mech. 34, 65-86 (1989).

[47] Apostol, D.A., Constantinescu, D.M., Marsavina, L., Linul, E. Particularities of the asymmetric four-point bending testing of polyurethane foams. U.P.B. Sci. Bull., Series D, 78 (2016).

[48] Bhattacharjee, D., Knott, J. F. Effect of mixed mode I and II loading on the fracture surface of polymethyl methacrylate ( PMMA ). Int. J. Fract. 72, 359-381 (1995).

[49] Maccagno, T.M., Knott, J. F. The Low Temperature Brittle Fracture Behavior of steel in Mixed modes I and II. Eng. Fract. Mech. 38, 111-128 (1991).

[50] Berto, F., Lazzarin, P., Ayatollahi, M. R. Brittle fracture of sharp and blunt V-notches in isostatic graphite under pure compression loading. Carbon N. Y. 63, 101-116 (2013).

[51] Berto, F., Campagnolo, A., Ayatollahi, M. R. Brittle Fracture of Rounded V-Notches in Isostatic Graphite under Static Multiaxial Loading. Phys. Mesomech. 18(4), 283-297 (2015).